

# Supporting Information for "Analysis and mapping of an updated terrestrial heat flow dataset"

F. Lucaleau<sup>1</sup>

<sup>1</sup>Université de Paris, Institut de physique du globe de Paris, CNRS, IGN, F-75005 Paris, France

## 1. Contents of this file

1. Text S1. to S4.
2. Tables S1 to S11
3. Figures S10 to S23

## 2. Additional Supporting Information (Files uploaded separately)

1. NGHF.csv: heat flow file. Signification of codes is given in tables S1 to S6.
2. HFgrid14.csv: preferred heat flow prediction on a  $0.5^\circ \times 0.5^\circ$  grid and with 14 observables.
3. hfb.pdf: references of the NGHF dataset

### S1. The NGHF data set

The NGHF data base is given with 6 metadata codes giving the geographic location (table S1), the geologic, tectonic or stratigraphic characteristics (table S2), the type of temperature gradient estimate (table S3), the type of thermal conductivity estimate (table S4), the type of correction eventually applied to heat flow (table S5) and the quality of data (table S6). Some proprietary or unpublished data have been removed from the csv file.

Figure S1 shows the distribution of heat flow data at the Earth surface according to the date of measurement (actually date of publication). The new measurements with respect to Pollack et al. (1993) are distributed all over the world and represent an enhancement of about 10% of the covered surface (red dots in figure S1). The surface covered by measurements depends on the resolution of the grid, and a comparison is shown in table S7 for  $5^\circ \times 5^\circ$ ,  $1^\circ \times 1^\circ$ ,  $0.5^\circ \times 0.5^\circ$  grids. The corresponding map distribution is shown in figure S2 for for  $5^\circ \times 5^\circ$  and  $0.5^\circ \times 0.5^\circ$  grids.

Figure S3 shows histograms of the heat flow distribution for a) continental values; b) oceanic values; c) oceanic values acquired before 1990; d) oceanic values acquired after 1990; e) oceanic values at a distance of 60 km to the next seamount and with a sediment thickness of at least 400 m; c) oceanic values of quality A. The black lines are the equivalent normal distributions with the median and L1 scale.

### S2. Oceanic heat flow

Figure S4 shows the variations of mantle thermal conductivity with temperature assumed in the numerical model of oceanic lithosphere cooling. The lattice contribution is given for 4 values of thermal conductivity at laboratory temperatures ( $3.4$  and  $6 \text{ W m}^{-1} \text{ K}^{-1}$ ) and the radiative contribution for two end-member models (Schatz & Simmons, 1972; Hofmeister, 1999). The model fitting observations for the sintered forsterite (Schatz & Simmons, 1972) corresponds to  $\simeq 5 \text{ W m}^{-1} \text{ K}^{-1}$ .

Figure S5 shows the effect of the accretion velocity on the surface heat flow, using 2D thermal models. As most of thermal models used for the cooling of oceanic lithosphere are 1D, it can be observed that this assumption is valid only for accretion velocities  $> 8 \text{ cm/y}$ .

The numerical model presented in the main paper is optimized for 6 parameters (thermal expansion coefficient, depth of the lower boundary condition, bottom heat flow or bottom temperature, accretion temperature, ridge subsidence and thermal conductivity of the mantle) by a Monte Carlo procedure. Five of these parameters are mapped by pairs of two and for the three selected models (figure S6, S7 and S8) in the range of parameter values. For the first model, which is best explained by a temperature boundary condition, the optimal range of mantle temperatures is constrained between  $1150\text{--}1250^\circ\text{C}$ . The coefficient of thermal expansion is also limited between  $2.6$  and  $3.1 \times 10^{-5} \text{ K}^{-1}$ . The thermal conductivity ranges between  $4.5$  and  $5.5 \text{ W m}^{-1} \text{ K}^{-1}$ , but is strongly linked to the depth of the lower boundary condition (figure S6).

For the second model (adjustment of subsidence at heat flow sites and adjustment of heat flow for old ages of the seafloor, 75–180 Ma), the preferred model is a constant heat flow at the lower boundary condition, which depth has no significant effect on other parameters values. The variation of these parameters is therefore represented as a function of mantle heat flow (figure S7). The range of optimal parameters is more or less similar, with slightly higher values for the coefficient of thermal expansion.

For the third model (adjustment of global subsidence with exclusion of locations where subsidence anomaly is  $> +2000\text{m}$  and adjustment of heat flow for old ages of the seafloor, 75–180 Ma), the maps of optimal parameters (figure S8) are similar to the second model.

### S3. Continental heat flow

#### S4. Prediction of heat flow using a similarity method

Figure S9 shows an example of weighted data collection at a location in France (longitude  $1.25^\circ$  and latitude  $44.75^\circ$ ) where no measurement exists. The collection is formed by heat flow values obtained at other locations in the world which have some similarity with this specific location.

Figures S10 to S23 represent several (not all used in this work) observables distribution on the Earth (lower part of figures) and the heat flow estimated from the single similarity (upper part of the figures). Some of them (age, seismic tomography,...) are more strongly correlated with heat flow, which gives well defined variations of heat flow at the surface. Some other observables (e.g. free air, distances,...) are not directly related to heat flow, but their combination with other observables improves the resolution. The following observables are displayed here:

1. Age of the ocean seafloor (Müller et al., 2008) (figure S10)
2. Tomography classification after Shapiro and Ritzwoller (2002) (figure S11)
3. Distance to volcanism (figure S12)
4. Earth lithosphere thickness (Conrad & Lithgow-Bertelloni, 2006) (figure S13)
5. Distance to mesozoic and cenozoic orogens (figure S14)
6. Classes of age (figure S15)
7. Average distance to seismogenic zones (figure S16)
8. Curie point depth (Li et al., 2017) divided into 21 classes of depths (table S8 and figure S17)

9. Free Air gravity classification (Sandwell & Smith, 2009) divided into 20 classes (table S9 and figure S18)
  10. Last Tectono-thermal age (USGS, 1997) (figure S19)
  11. UNESCO stratigraphy (CCGM/CGMW, 2000) divided into 32 classes (table S11 and figure S20)
  12. Distance to Cenozoic rifts (figure S21)
  13. Earth topography and bathymetry (Kautz, 2017) (figure S22)
  14. Average distance to Archean (figure S23)
- [.usgs.gov/data/crust/age.html](http://usgs.gov/data/crust/age.html)

## References

- CCGM/CGMW. (2000). *Geological map of the world at 1:25 000 000*. CD Rom. Retrieved from <http://ccgm.free.fr/cartes\monde\gb.html> (2nd edition)
- Conrad, C. P., & Lithgow-Bertelloni, C. (2006). Influence of continental roots and asthenosphere on plate-mantle coupling. *Geophysical Research Letters*, 33(5). doi: 10.1029/2005GL025621
- Hofmeister, A. M. (1999). Mantle values of thermal conductivity and the geotherm from phonon lifetimes. *Science*, 283, 1699-1706. doi: 10.1126/science.283.5408.1699
- Kautz, S. (2017). *Global 30 arc-second elevation (gtopo30)*. U.S. Geological Survey. doi: 10.5066/F7DF6PQS
- Li, C.-F., Lu, Y., & Wang, J. (2017). A global reference model of curie-point depths based on EMAG2. *Scientific Reports*, 7(1). doi: 10.1038/srep45129
- Müller, R. D., Sdrolias, M., Gaina, C., & Roest, W. R. (2008, April). Age, spreading rates, and spreading asymmetry of the world's ocean crust. *Geochemistry Geophysics Geosystems*, 9(4), Q04006. doi: 10.1029/2007GC001743
- Pollack, H. N., Hurter, S. J., & Johnston, J. R. (1993). Heat loss from the earth's interior: analysis of the global data set. *Review of Geophysics and Space Physics*, 31, 267-280. doi: 10.1029/93RG01249
- Sandwell, D. T., & Smith, W. H. F. (2009). Global marine gravity from retracked Geosat and ERS-1 altimetry: Ridge segmentation versus spreading rate. *Journal of Geophysical Research*, 114, B01411-B01411. doi: 10.1029/2008jb006008
- Schatz, J. F., & Simmons, G. (1972). Thermal conductivity of the earth material at high temperatures. *Journal of Geophysical Research*, 77(35), 6966-6983. doi: 10.1029/JB077i035p06966
- Shapiro, N. M., & Ritzwoller, M. H. (2002). Monte-Carlo inversion for a global shear-velocity model of the crust and upper mantle. *Geophysical Journal International*, 151, 88—105. doi: 10.1046/j.1365-246x.2002.01742.x
- Stein, C. S., & Stein, S. (1992). A model for the global variation in oceanic depth and heat flow with lithospheric age. *Nature*, 359, 123-129. doi: 10.1038/359123a0
- USGS. (1997). *Geologic province and thermo-tectonic age maps*. Retrieved from <https://earthquake.usgs.gov/data/crust/age.html>



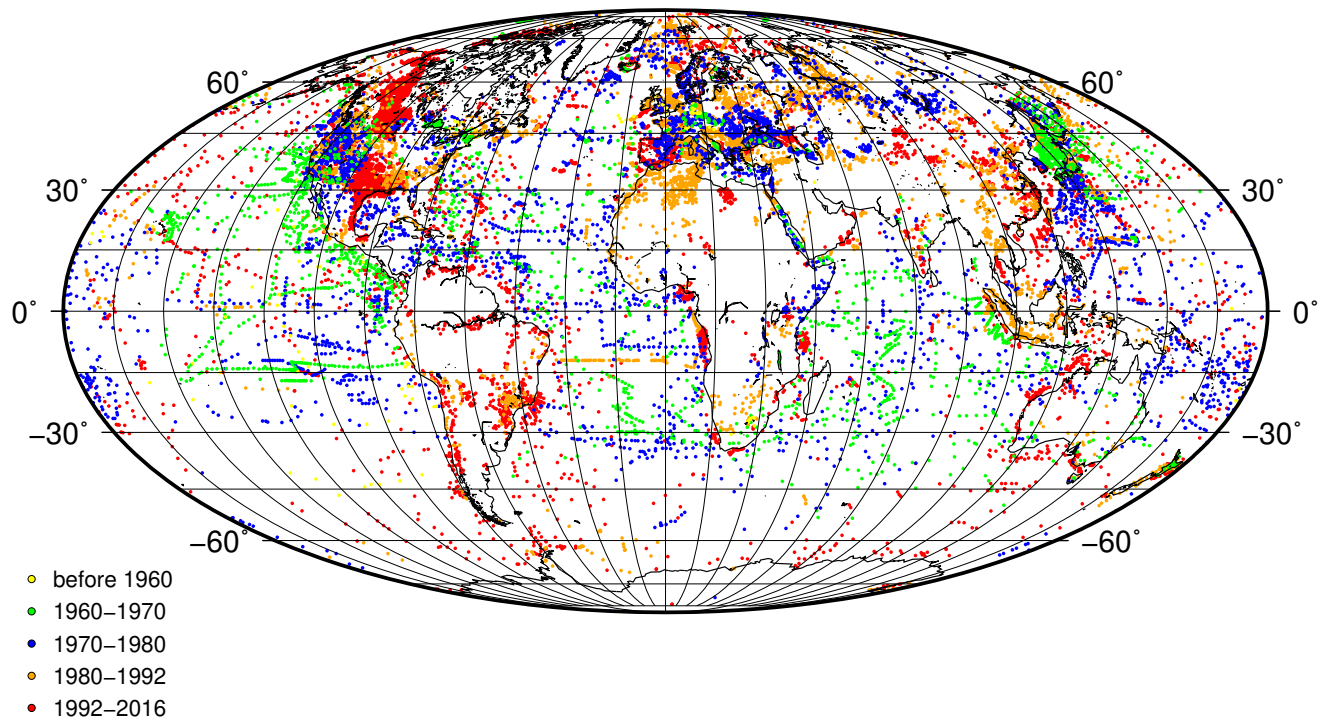


**Figure S1.** Distribution of NGHF data on the Earth according to publication date (coloured dots)

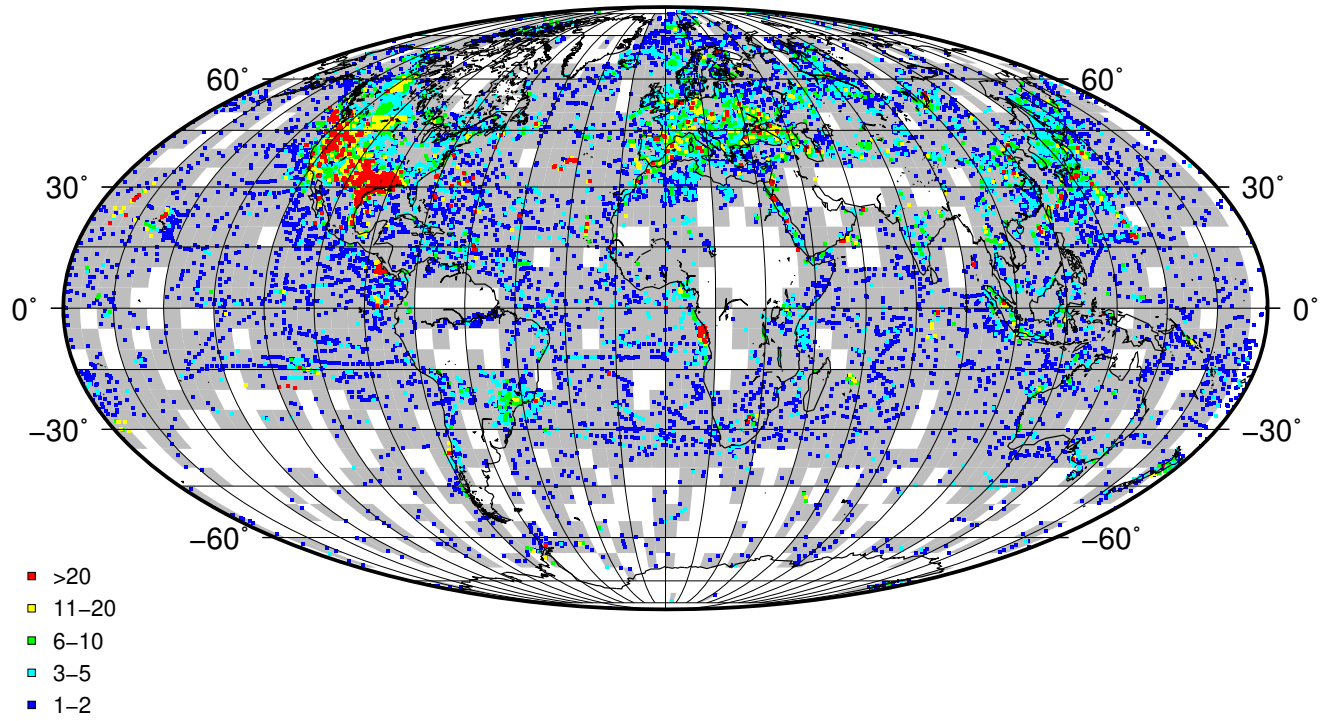


**Figure S2.** Distribution of NGHF data on a  $0.5^\circ \times 0.5^\circ$  grid (colours show the number of measurements in each cell) and on a  $5^\circ \times 5^\circ$  grid (grey pattern).

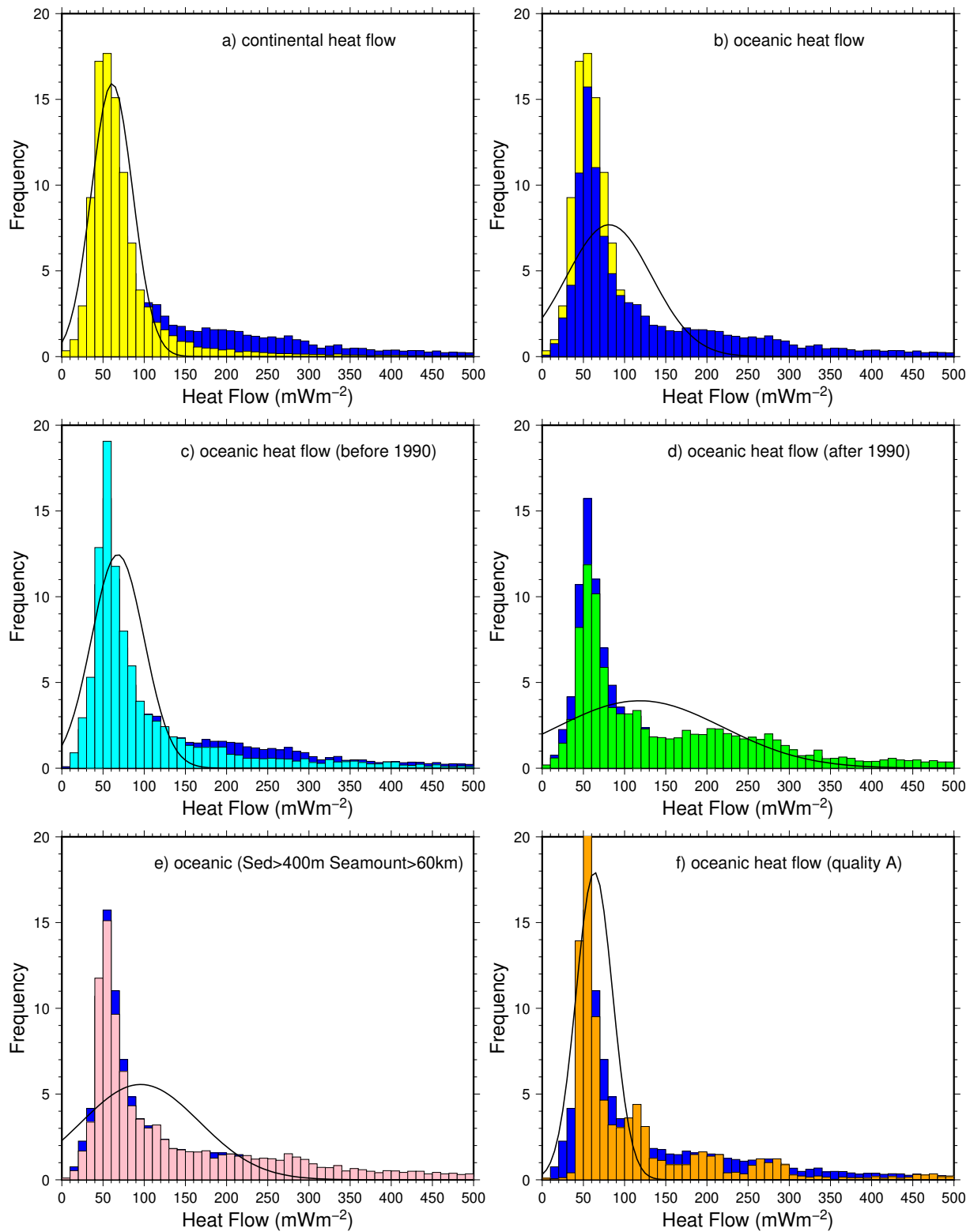


**Figure S3.** Distribution of heat flow in the NGHF data base

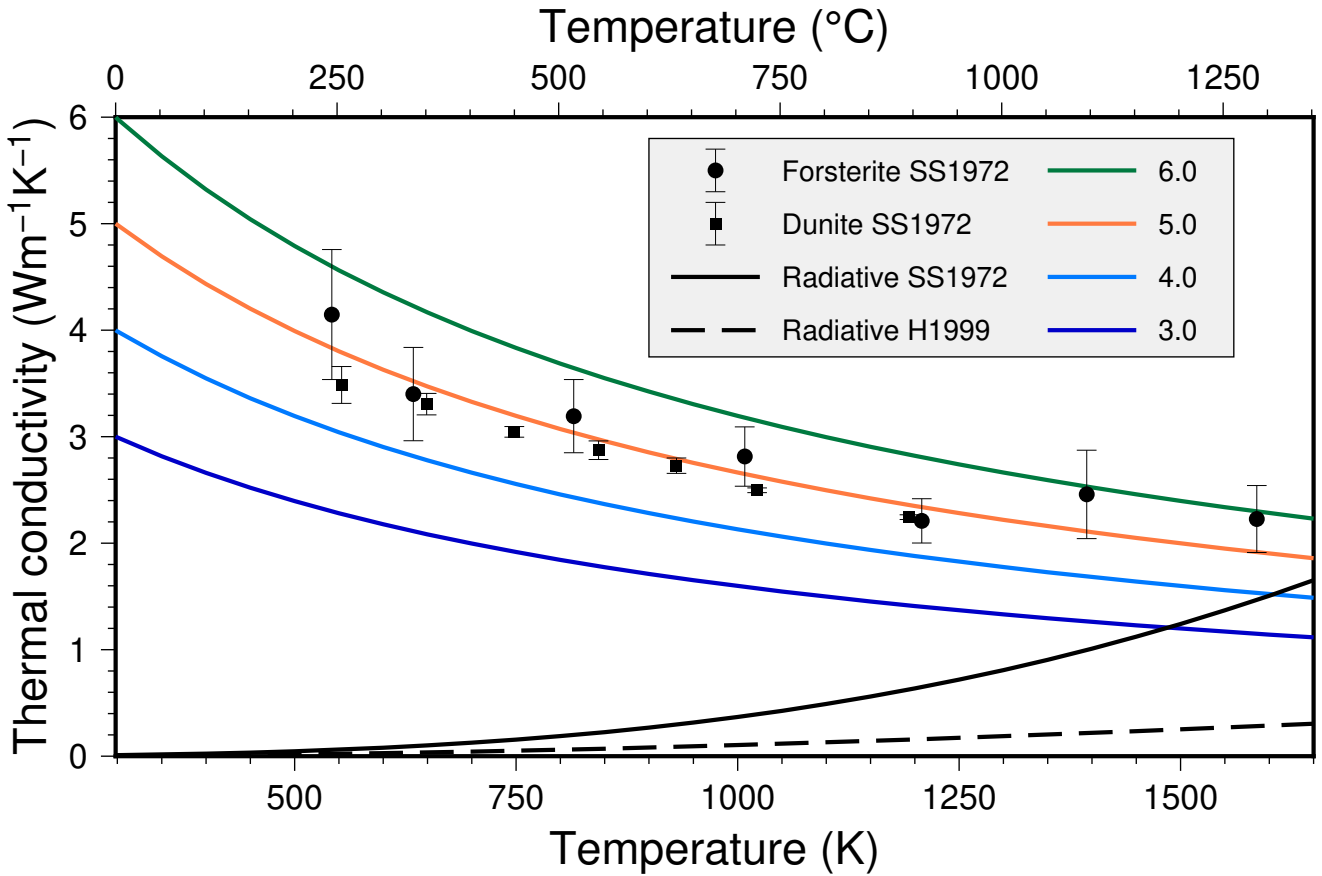


**Figure S4.** Conductivity variations with temperature in the numerical models. The colored lines correspond respectively to mantle conductivity of 6.0, 5.0, 4.0 and 3.0  $\text{Wm}^{-1}\text{K}^{-1}$  at 25 °C. Black circles and squares are the experimental values with their uncertainties respectively for sintered forsterite and olivine (Schatz & Simmons, 1972) and the black line is the radiative contribution from the same study  $\lambda_{\text{radiative}} = 3.68 \times 10^{-10} T_{\text{abs}}^3$ . The dash line is the radiative contribution from Hofmeister (1999).

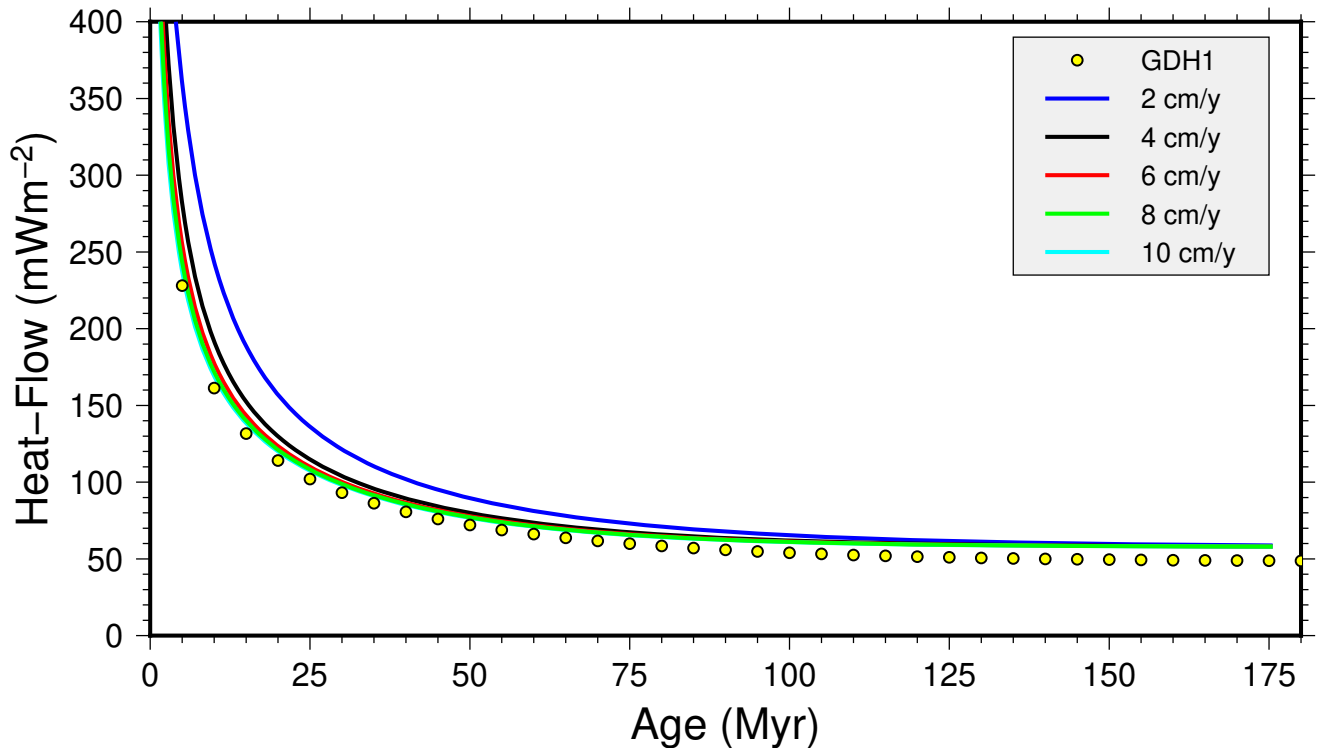


**Figure S5.** Variations of heat flow with age for different accretion velocities and comparison with GDH1 (Stein & Stein, 1992). The lateral heat conduction effect becomes negligible for 8 cm/y.

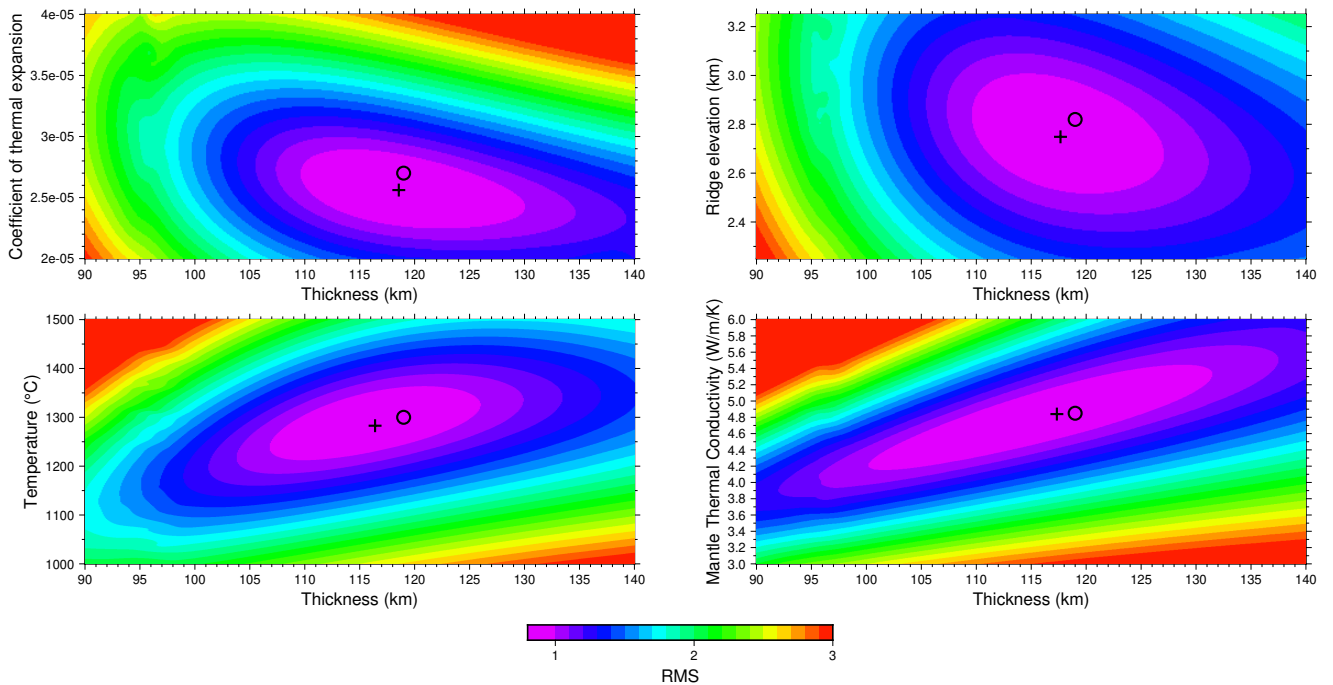


**Figure S6.** Misfit maps for the first oceanic lithosphere cooling model (adjustment of global subsidence and heat flow). Temperature at the bottom boundary condition, thermal conductivity of the mantle, thermal expansion coefficient and ridge elevation are shown independently as functions of the bottom boundary condition depth. Crosses are best models in the 2D space, circles represent the best model ( $L = 119$  km,  $T_L = 1300^\circ\text{C}$ ,  $\lambda_L = 4.85 \text{ W m}^{-1}\text{K}^{-1}$ ,  $\alpha = 2.70 \times 10^{-5} \text{ K}^{-1}$ ,  $h_0 = 2.82$  km).

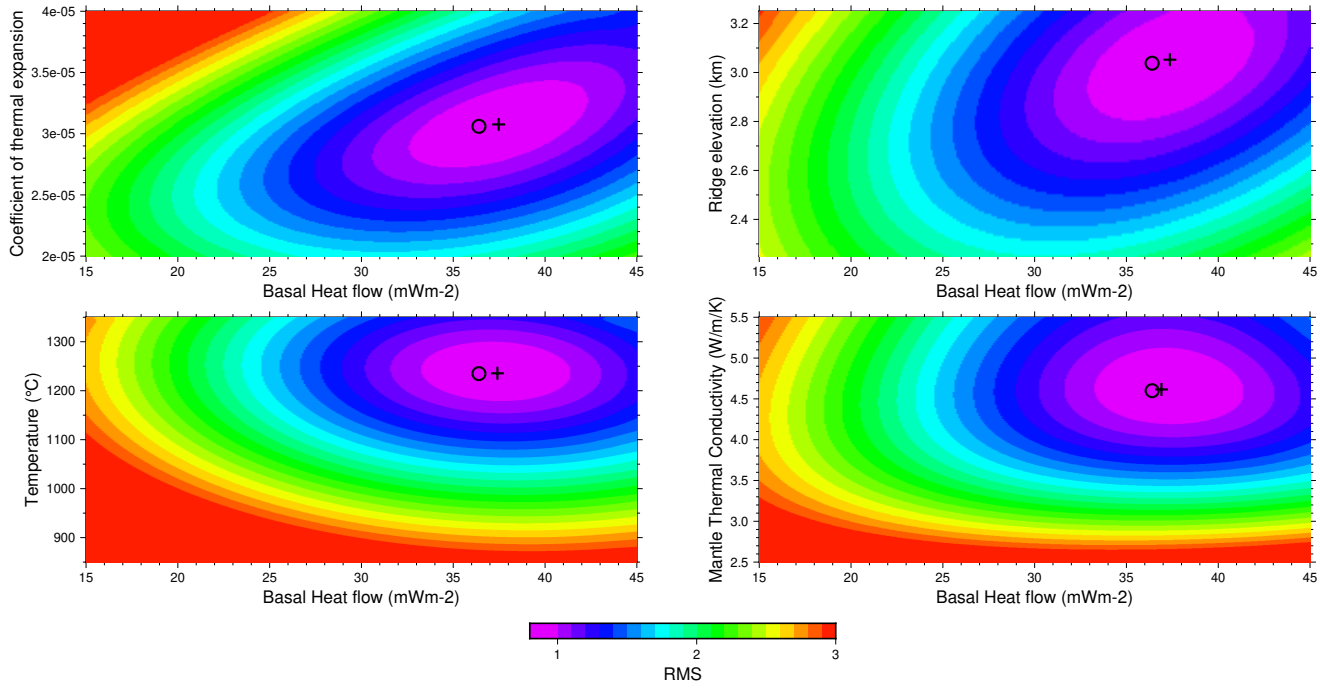


**Figure S7.** Misfit maps for the second oceanic lithosphere cooling model (adjustement of subsidence at heat flow sites and heat flow). Temperature at the bottom boundary condition, thermal conductivity of the mantle, thermal expansion coefficient and ridge elevation are shown independently as functions of the bottom boundary condition heat flow. Crosses are best models in the 2D space, circles represent the best model ( $L = 114$  km,  $q_L = 36.4$  mWm $^{-2}$ ,  $T_L = 1235^\circ\text{C}$ ,  $\lambda_L = 4.60$  Wm $^{-1}\text{K}^{-1}$ ,  $\alpha = 3.06 \times 10^{-5}$  K $^{-1}$ ,  $h_0 = 3.04$  km).

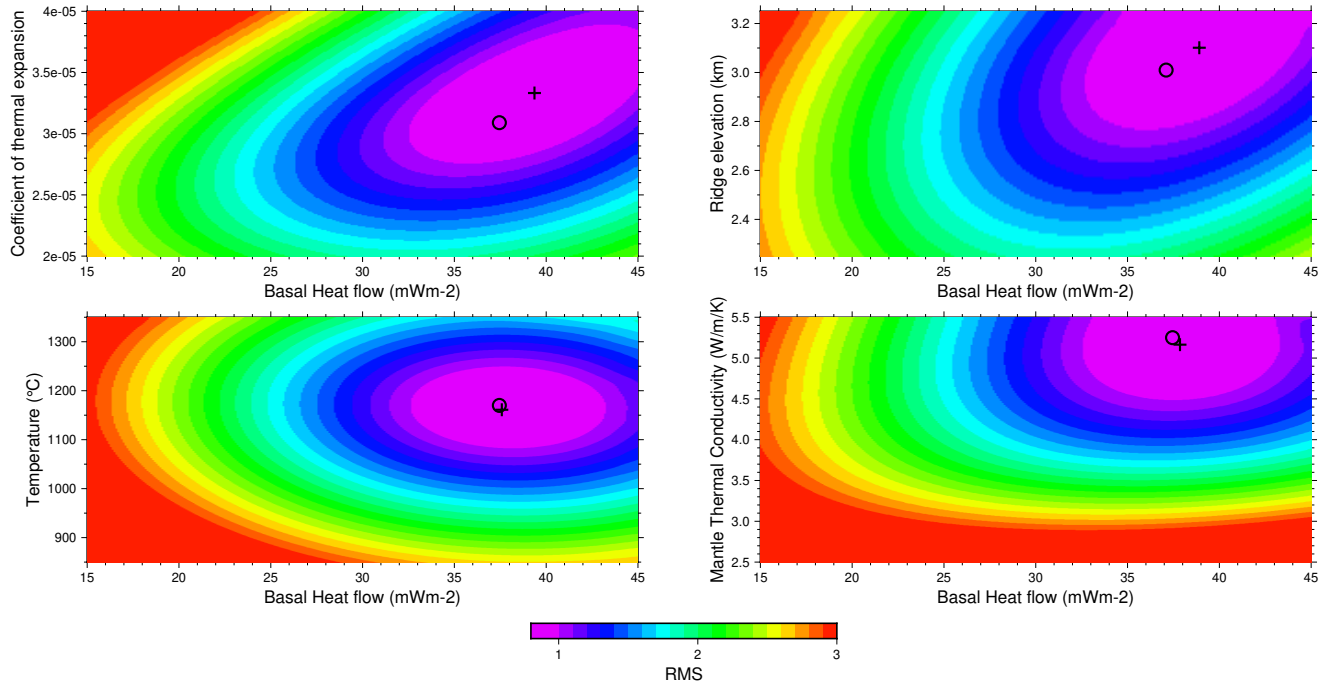


**Figure S8.** Misfit maps for the third oceanic lithosphere cooling model (adjustement of global subsidence without anomalous locations and heat flow). Temperature at the bottom boundary condition, thermal conductivity of the mantle, thermal expansion coefficient and ridge elevation are shown independently as functions of the bottom boundary condition heat flow. Crosses are best models in the 2D space, circles represent the best model ( $L = 118$  km,  $q_L = 37.1$  mWm $^{-2}$ ,  $T_L = 1170^\circ\text{C}$ ,  $\lambda_L = 5.25$  Wm $^{-1}\text{K}^{-1}$ ,  $\alpha = 3.09 \times 10^{-5}$  K $^{-1}$ ,  $h_0 = 3.01$  km).

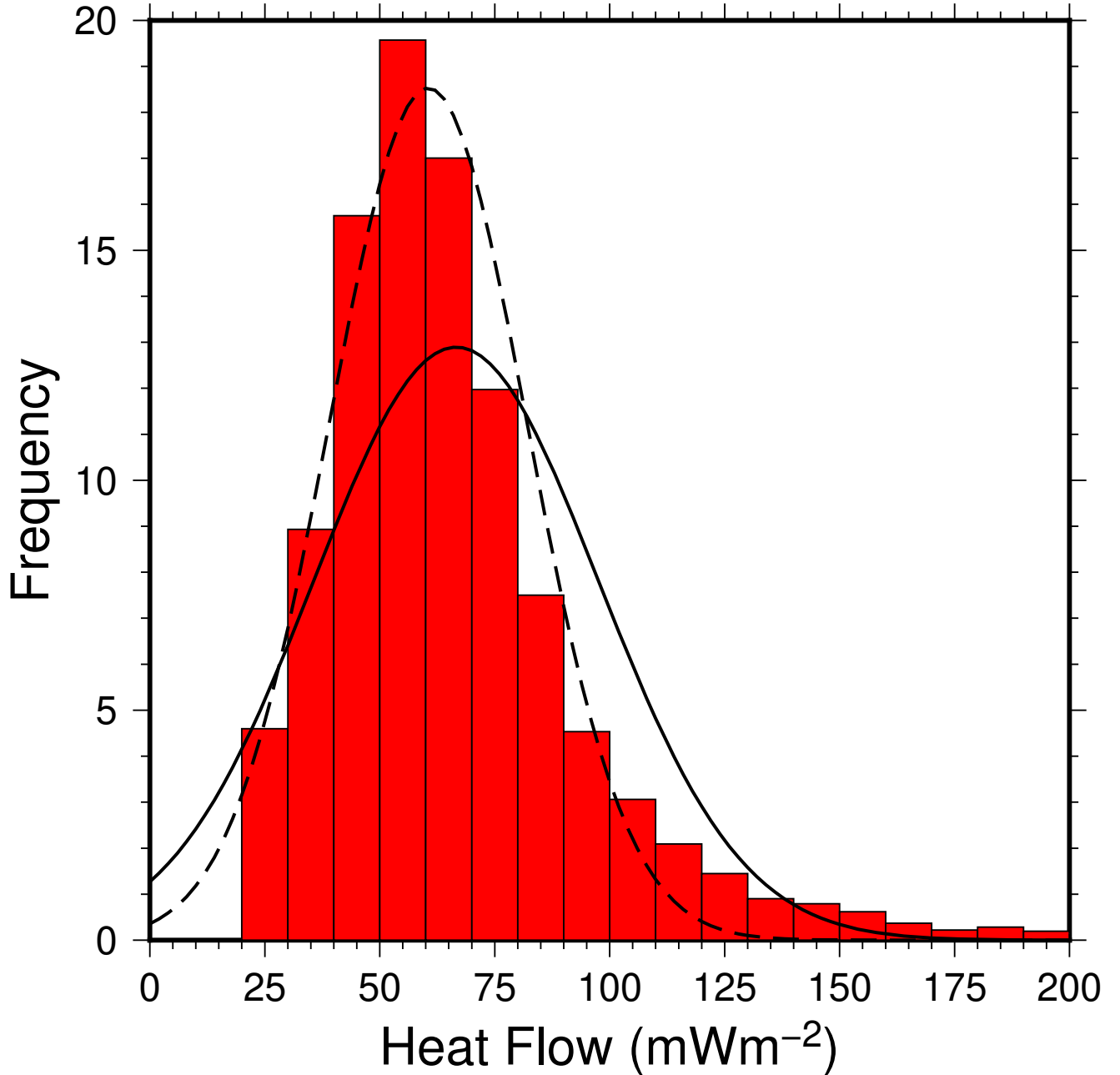


**Figure S9.** Histogram of similar data collected for a location in France (Longitude: 1.2500 and latitude: 44.7500), using a weight  $w_i = 10^{N_{sim}}$ . The black line is the equivalent normal distribution with the mean and standard deviation and the dashed lined is the equivalent normal distribution with the median and L1 scale ( $60.1 \pm 3.5 mWm^{-2}$ ).

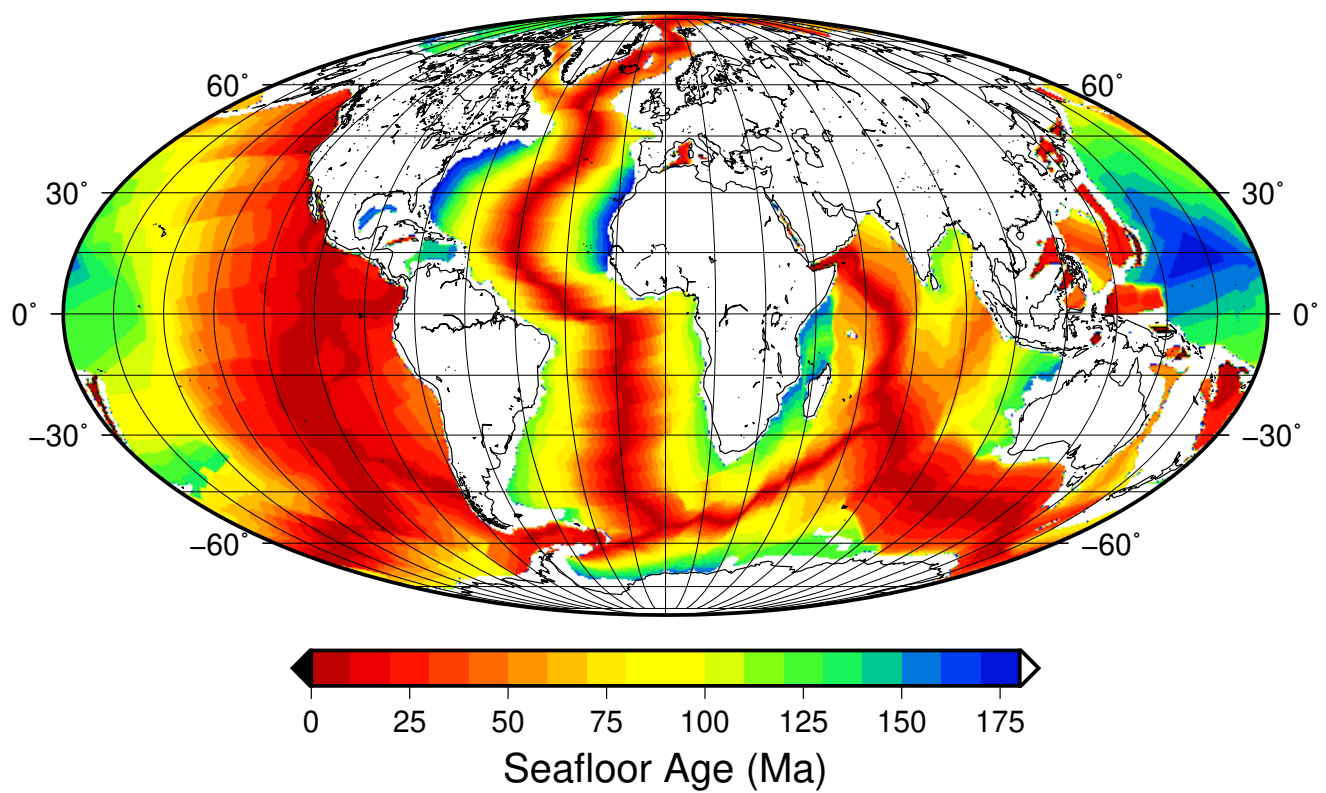
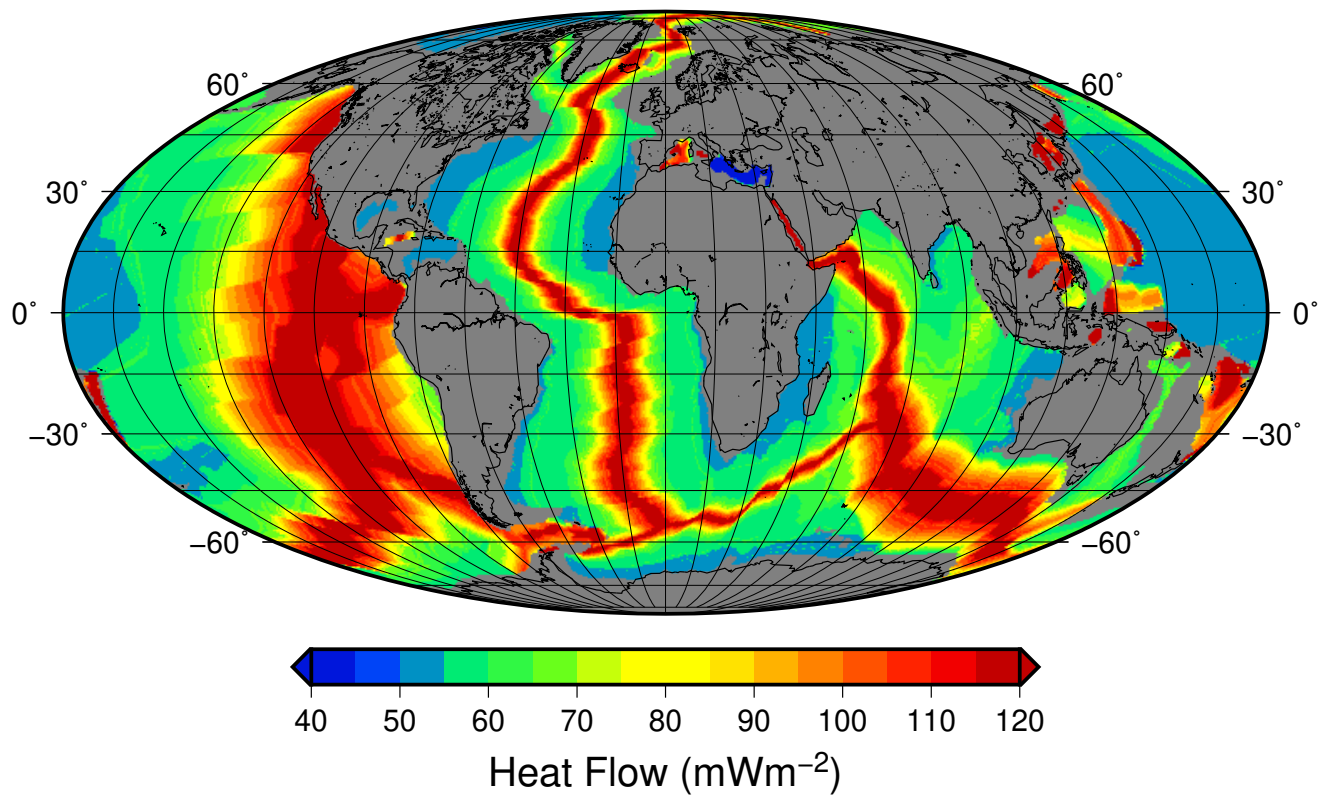


**Figure S10.** Age of the ocean seafloor (Müller et al., 2008)

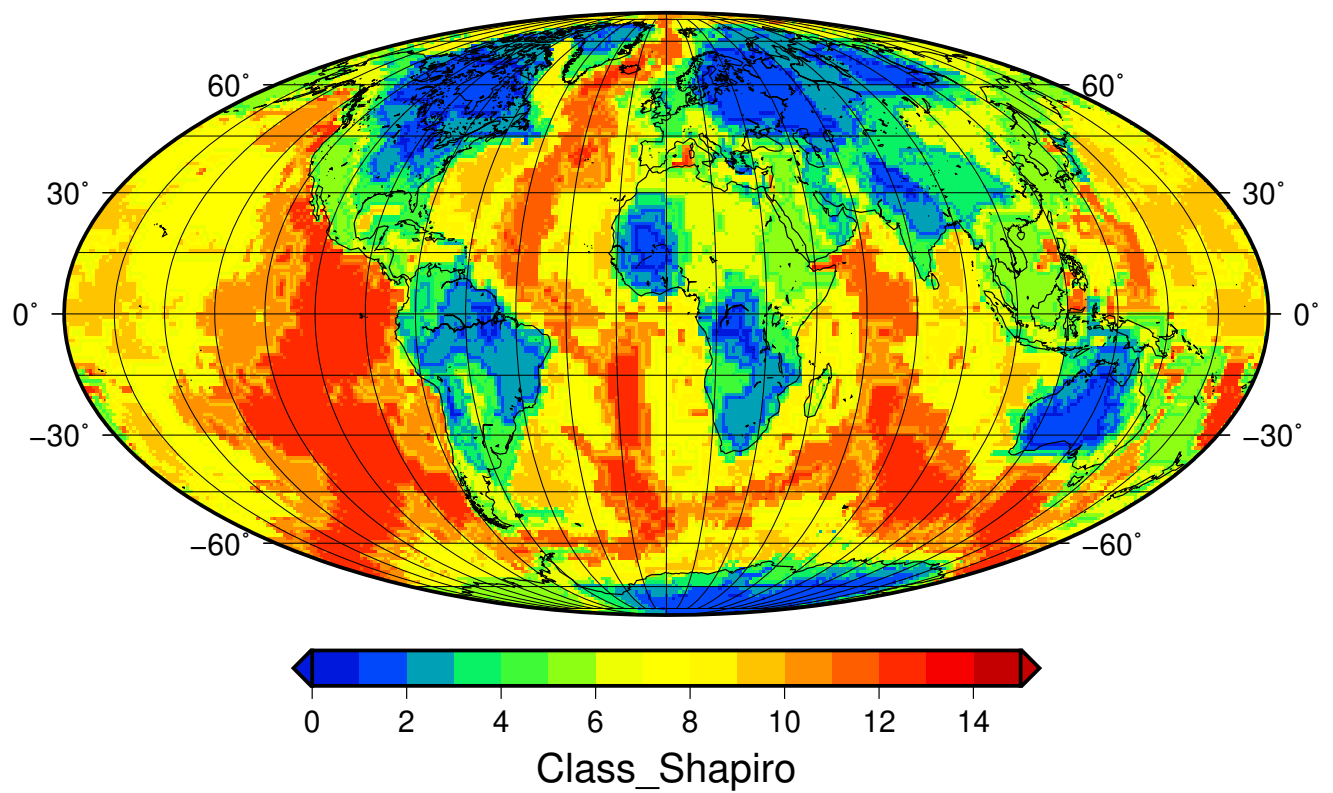
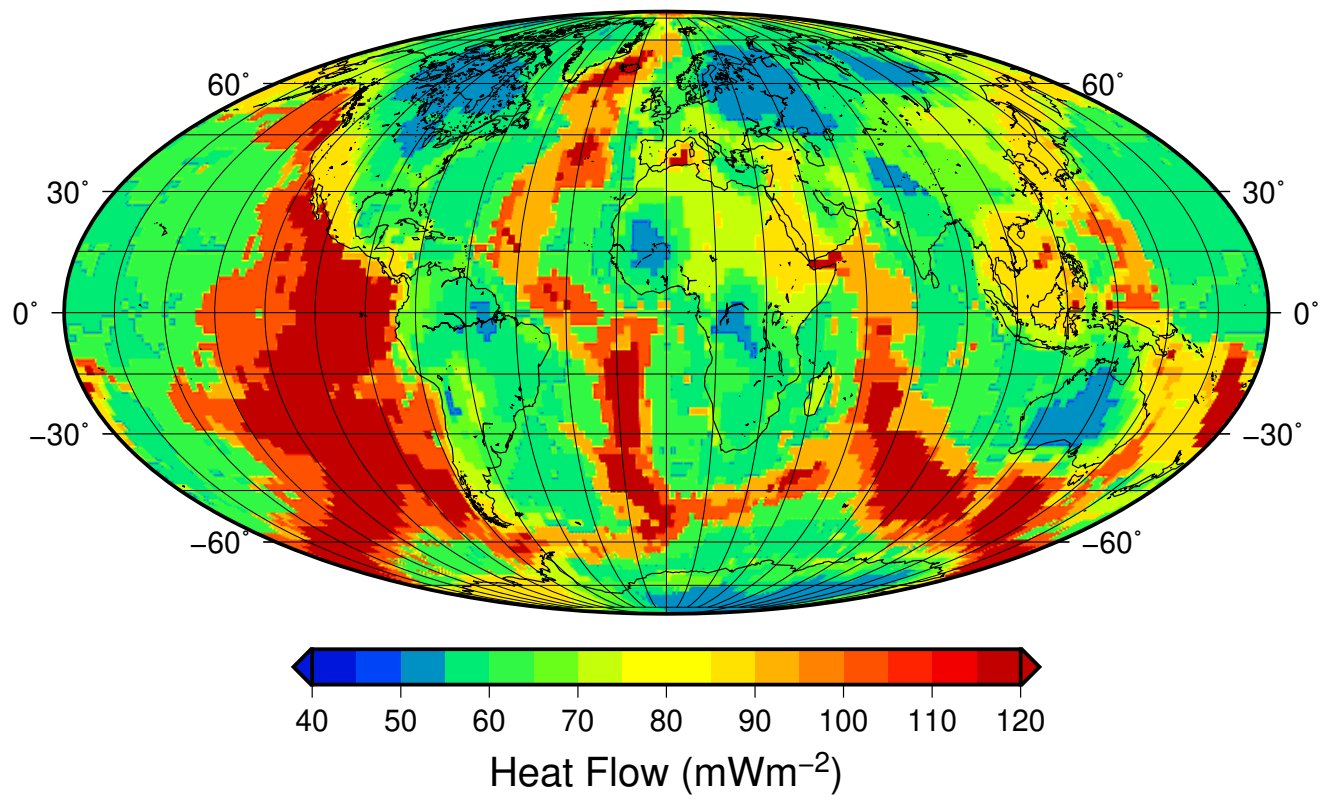


**Figure S11.** Tomography classification after Shapiro and Ritzwoller (2002)

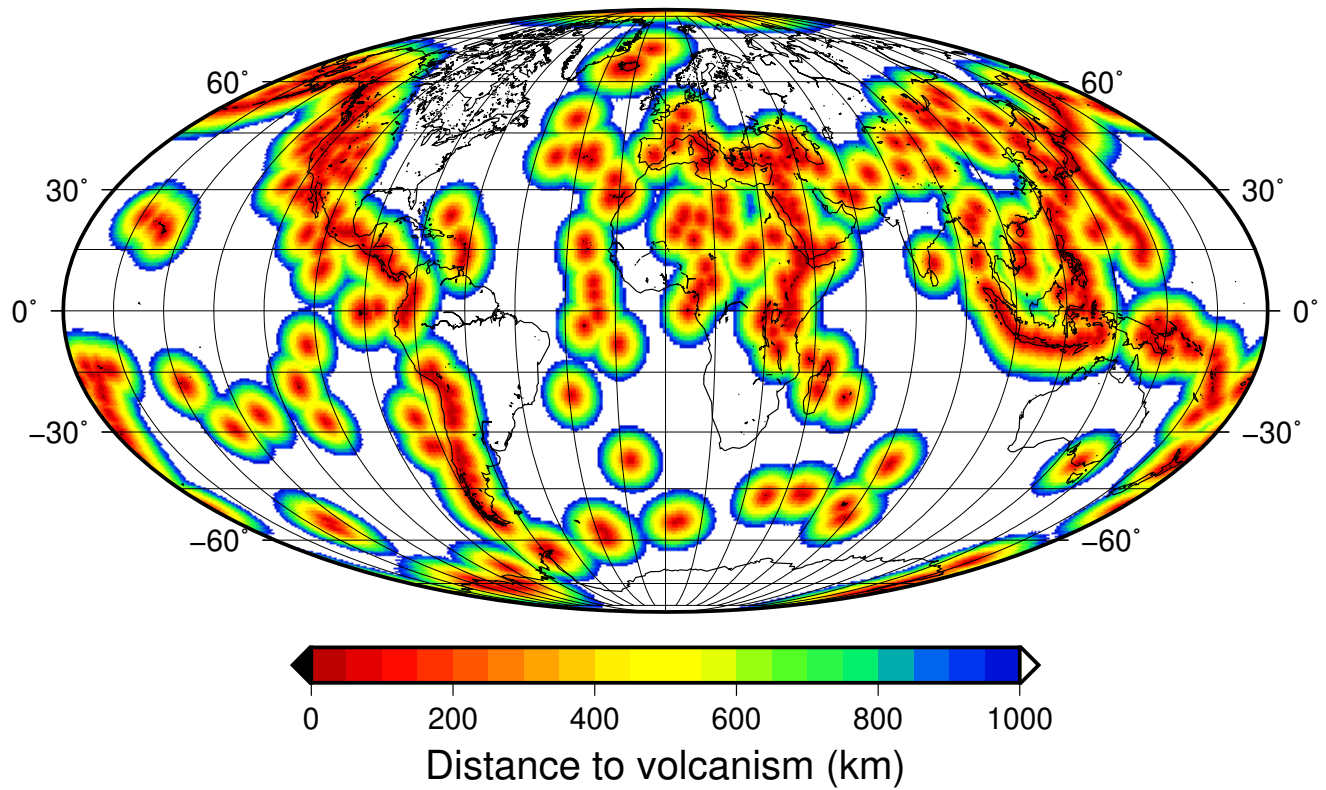
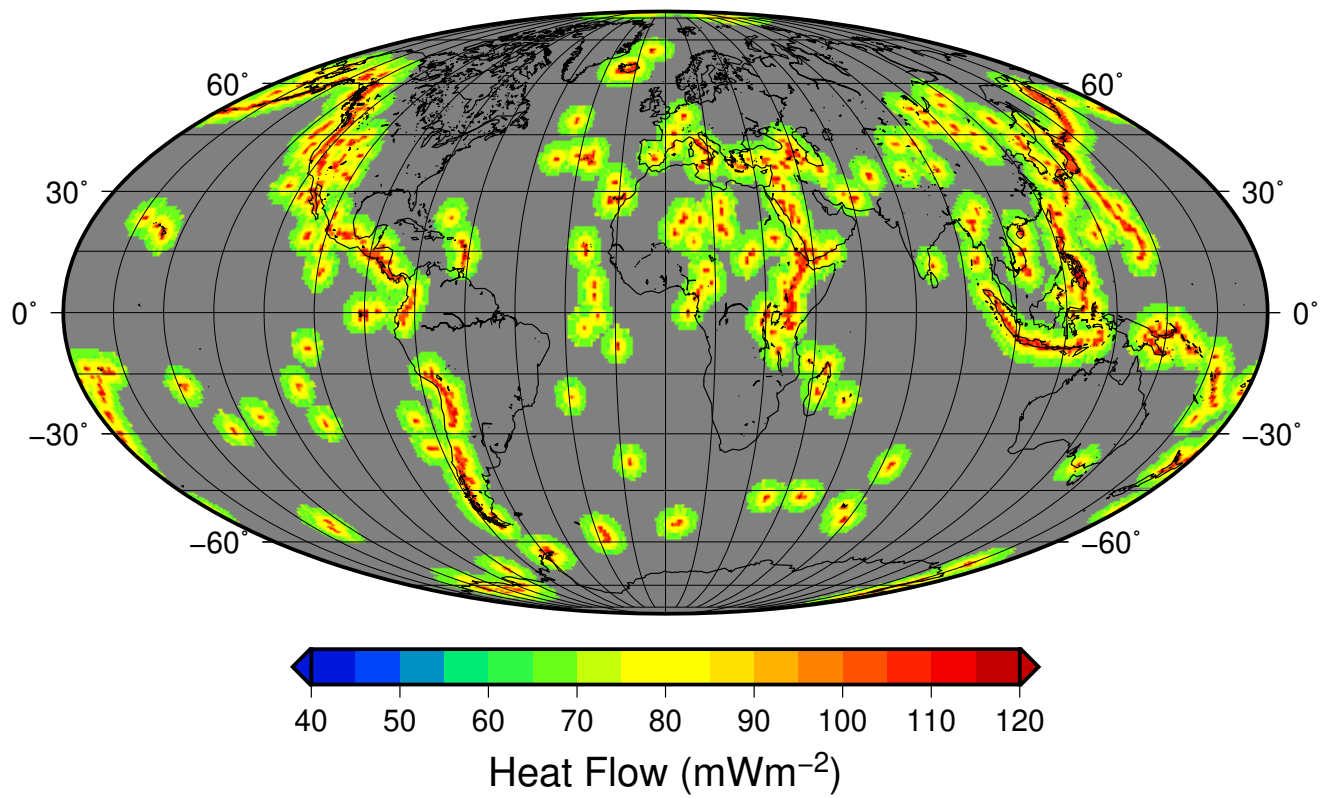


**Figure S12.** Distance to volcanism

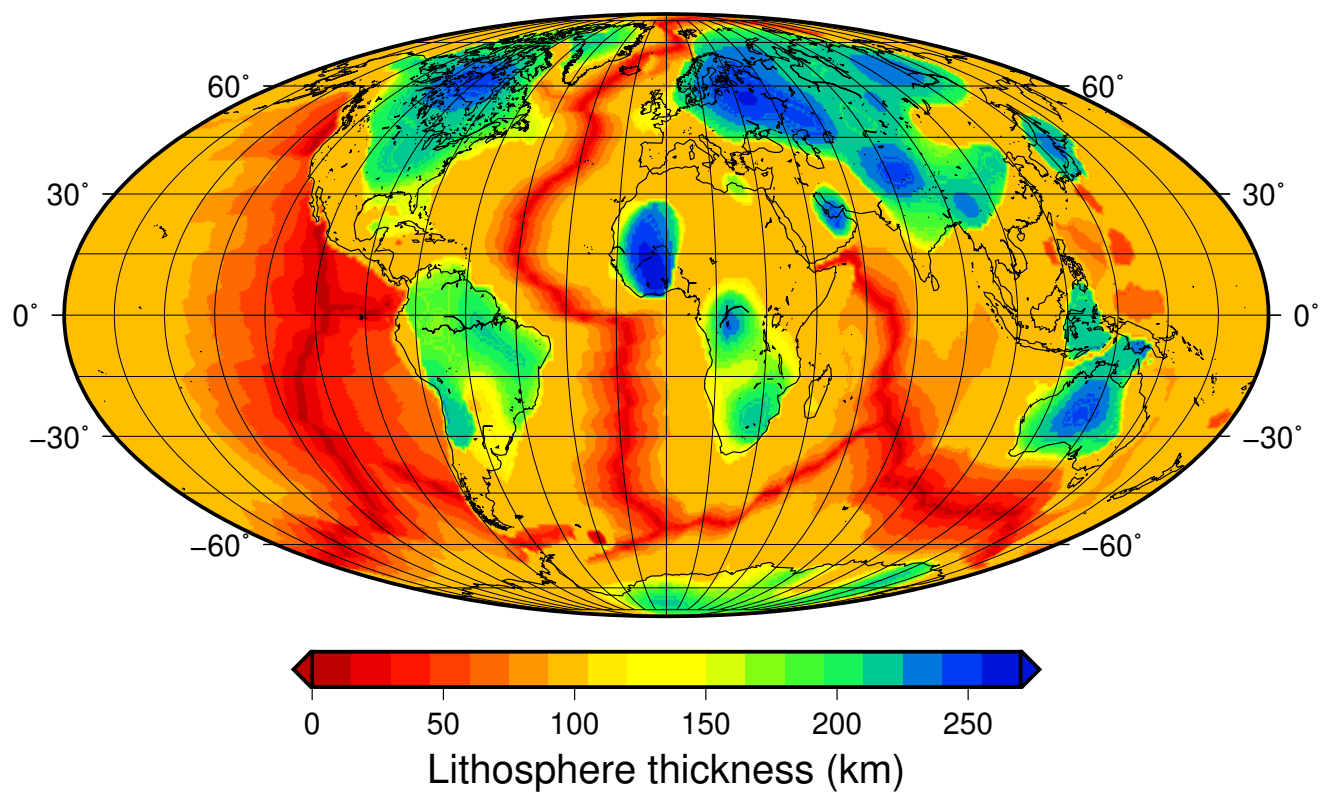
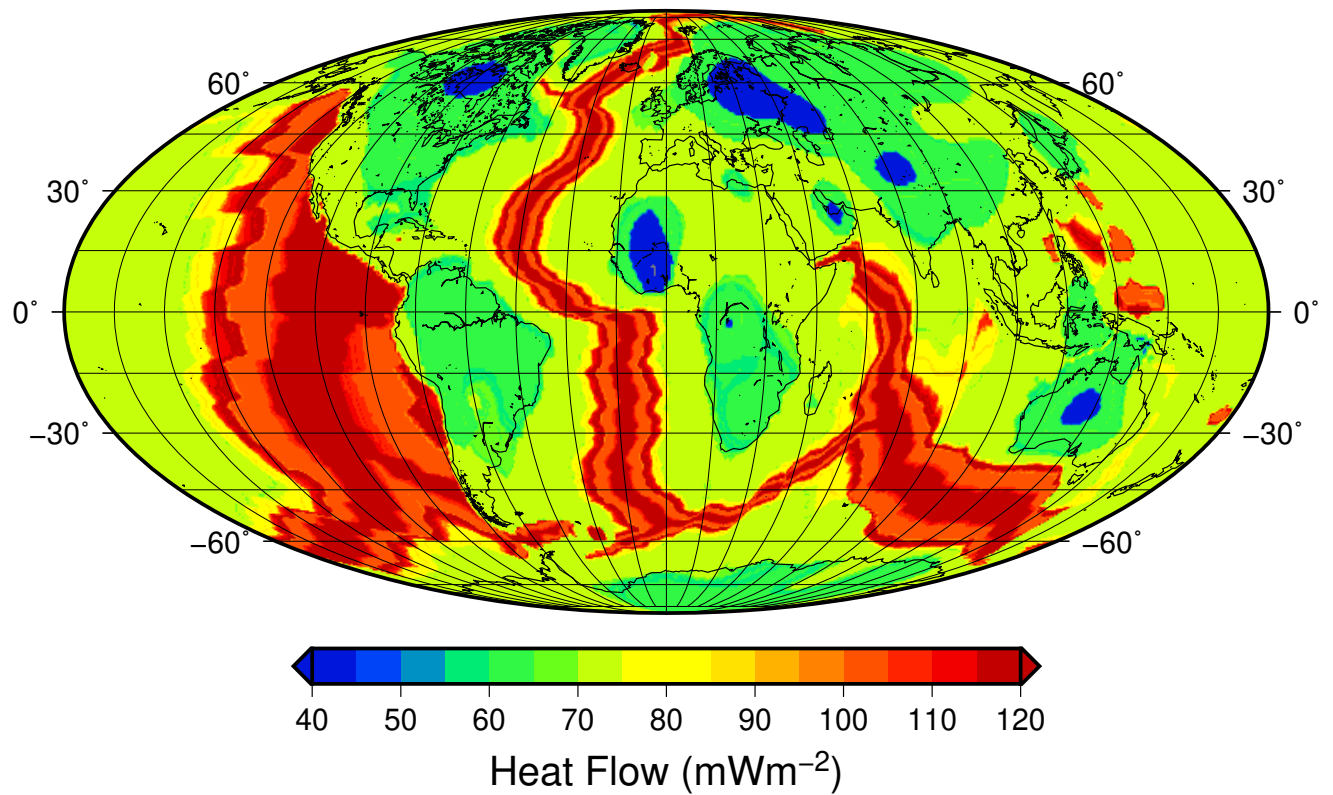
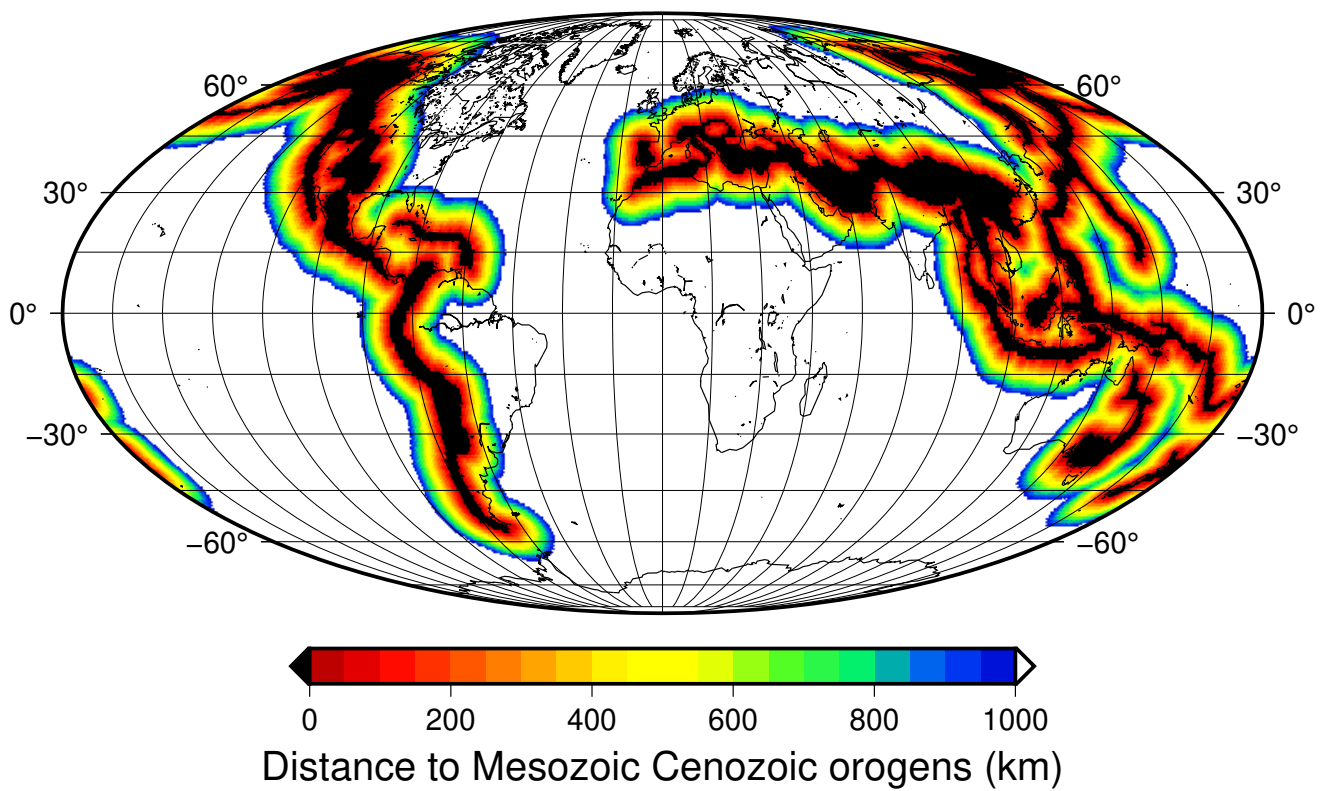
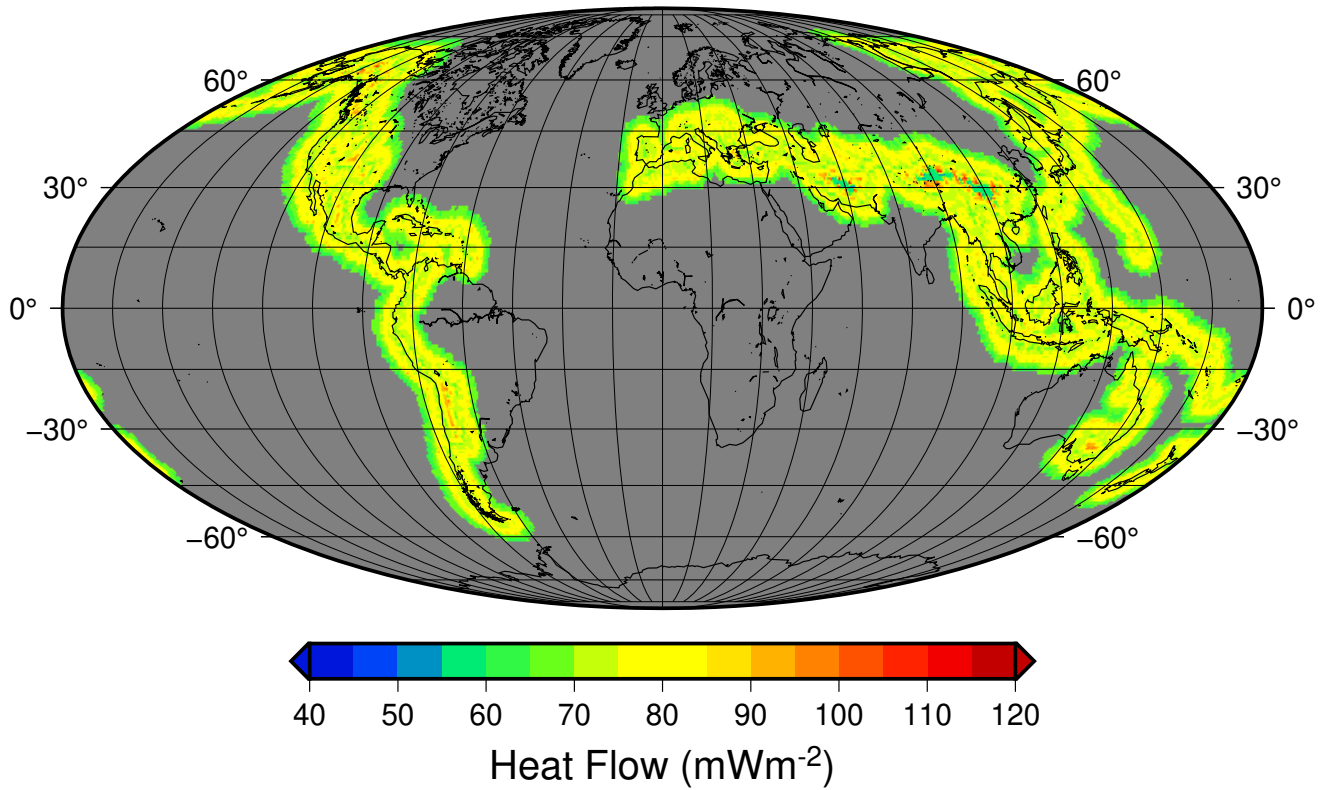


Figure S13. Earth lithosphere thickness (Conrad & Lithgow-Bertelloni, 2006)



**Figure S14.** Distance to mesozoic and cenozoic orogens

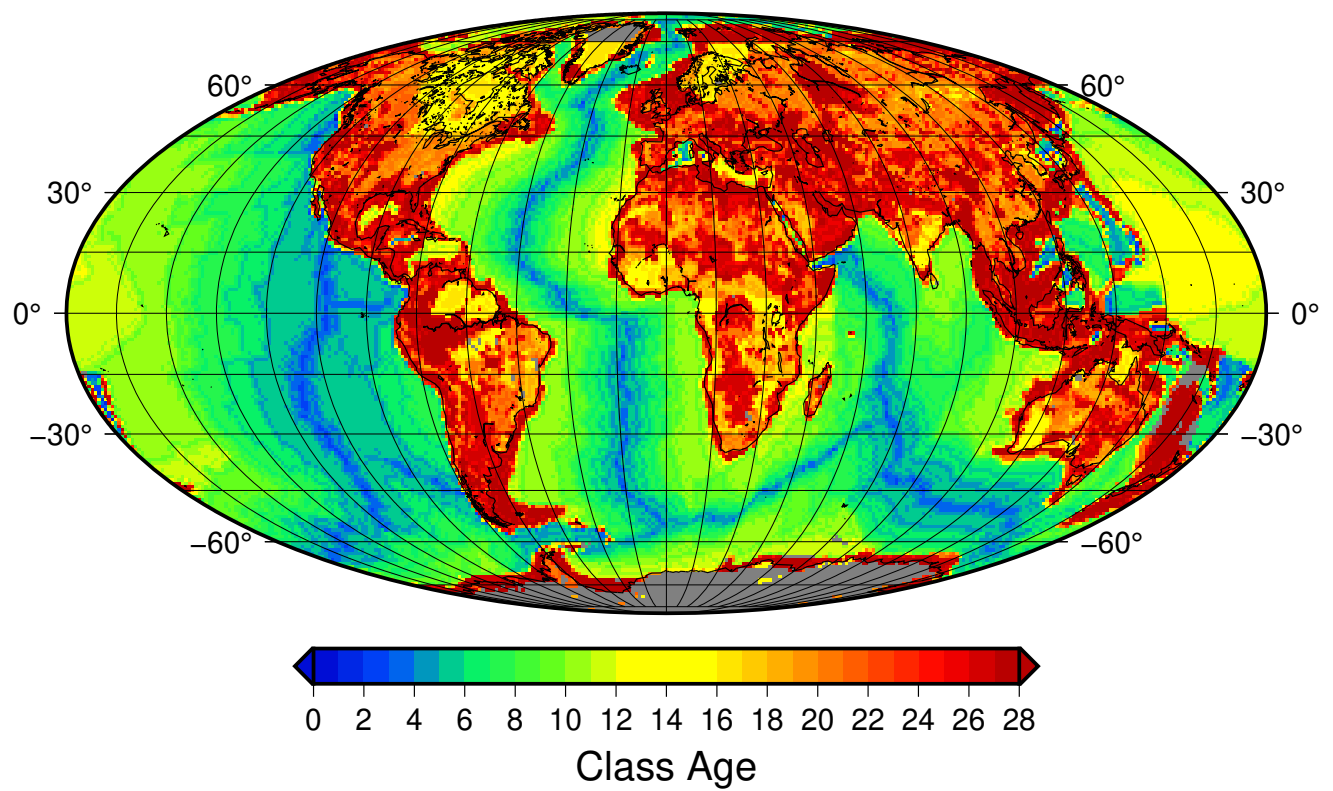
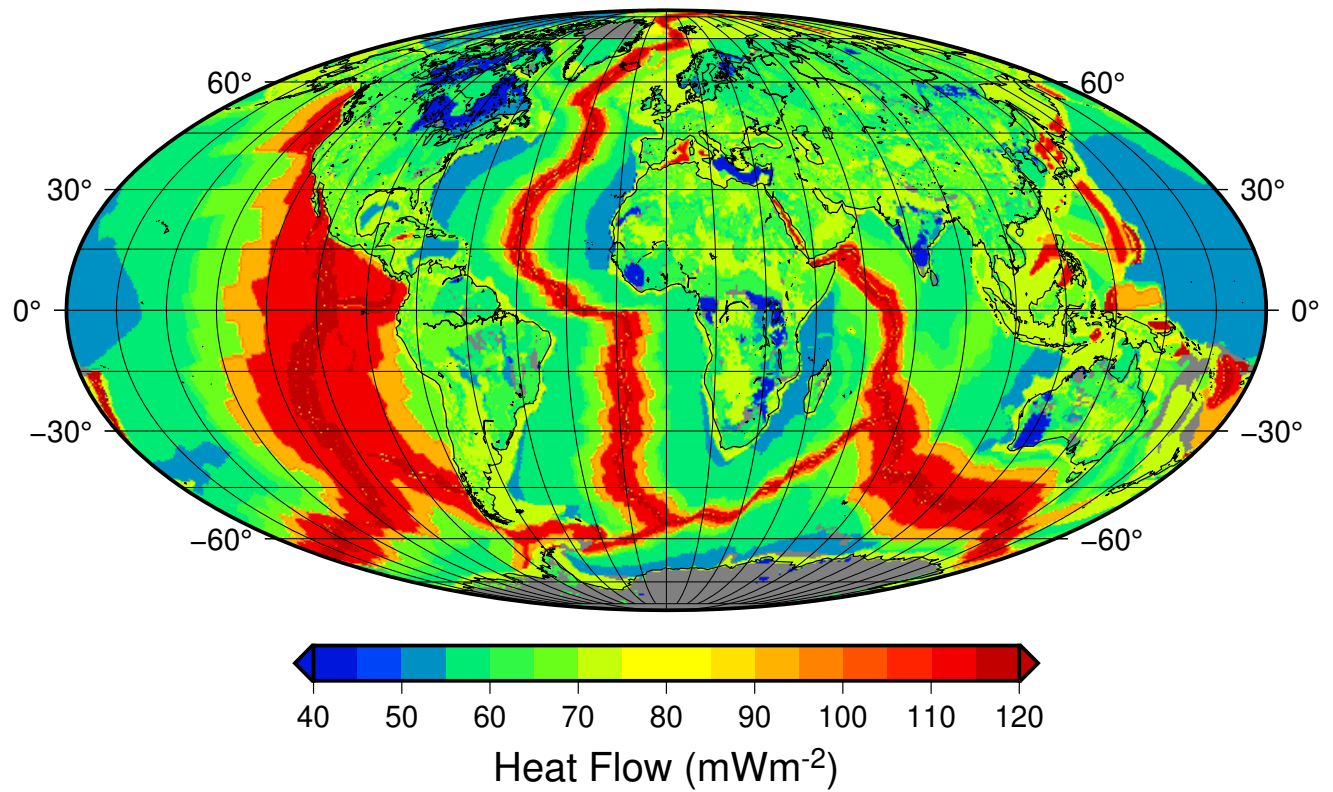
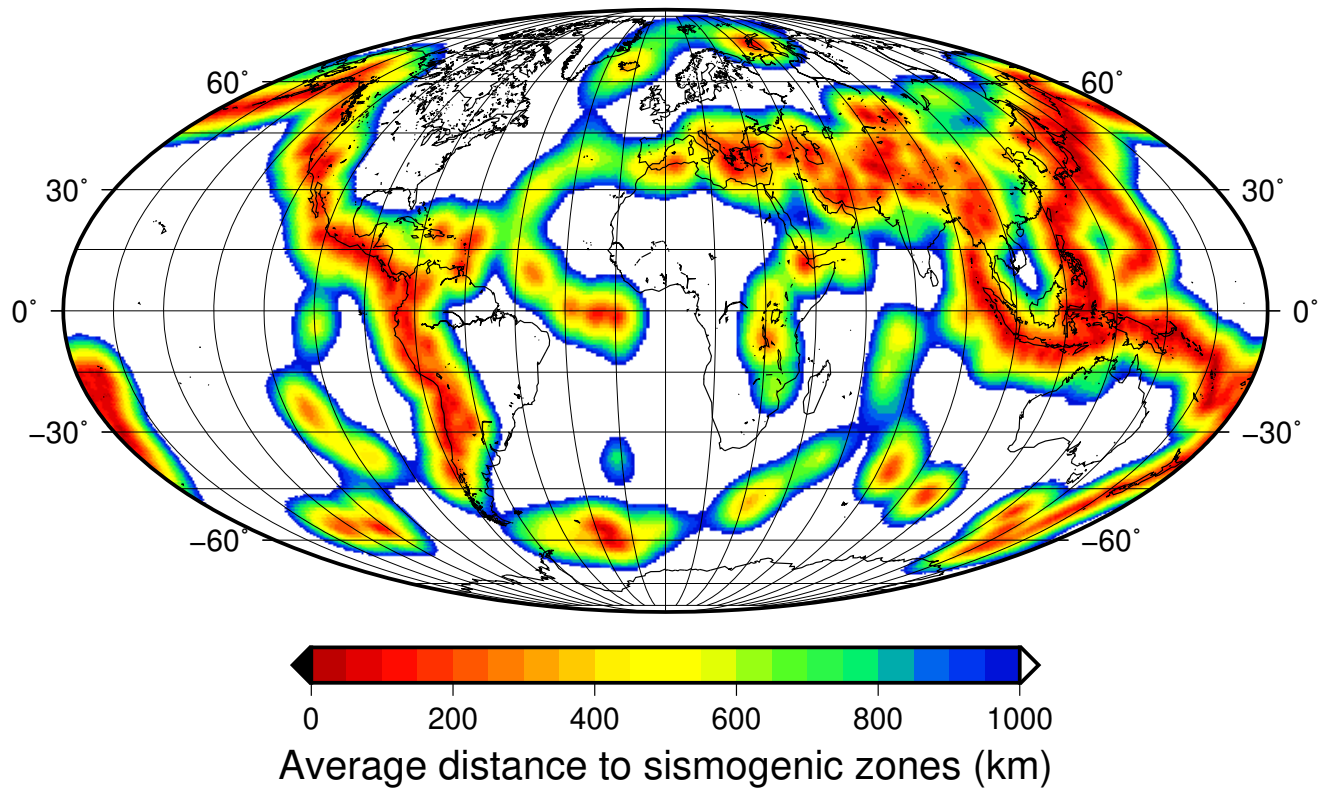
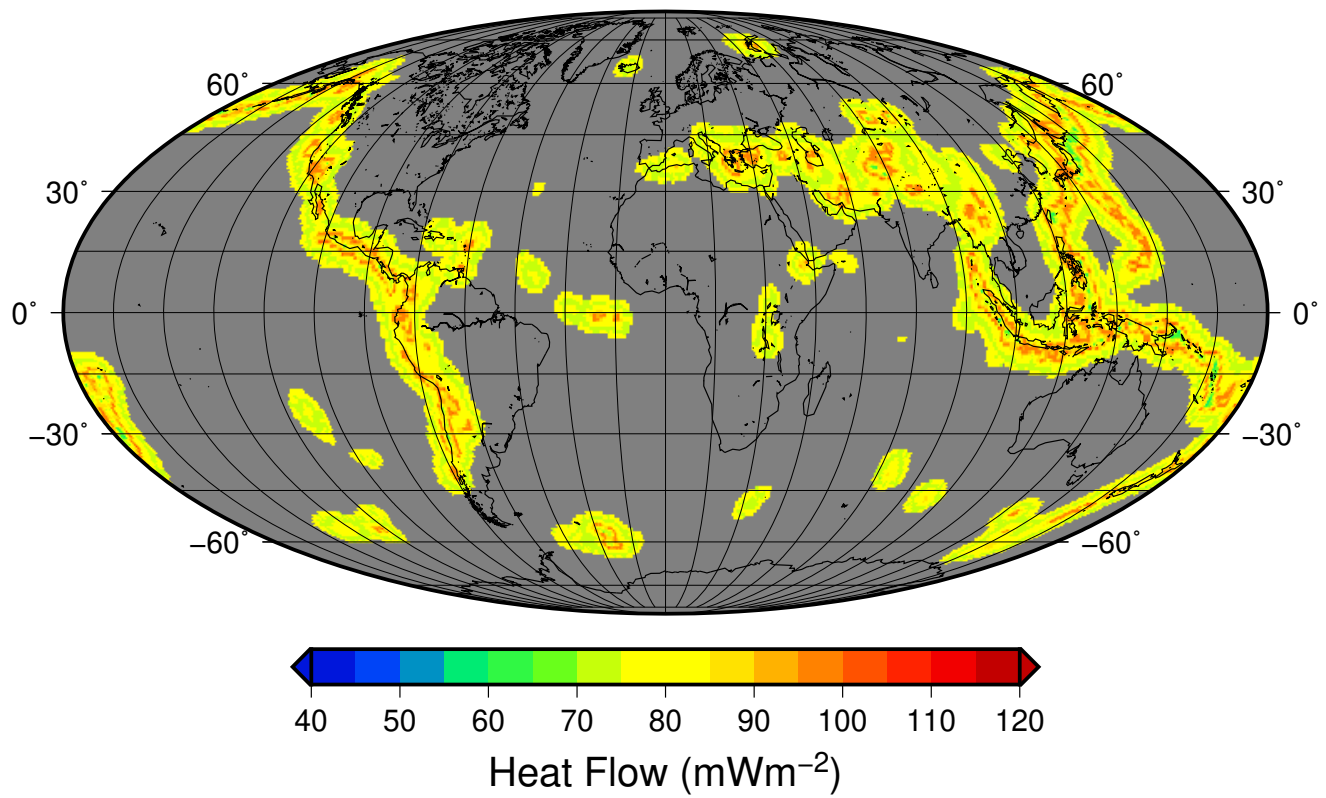


Figure S15. Classes of age



**Figure S16.** Average distance to seismogenic zones

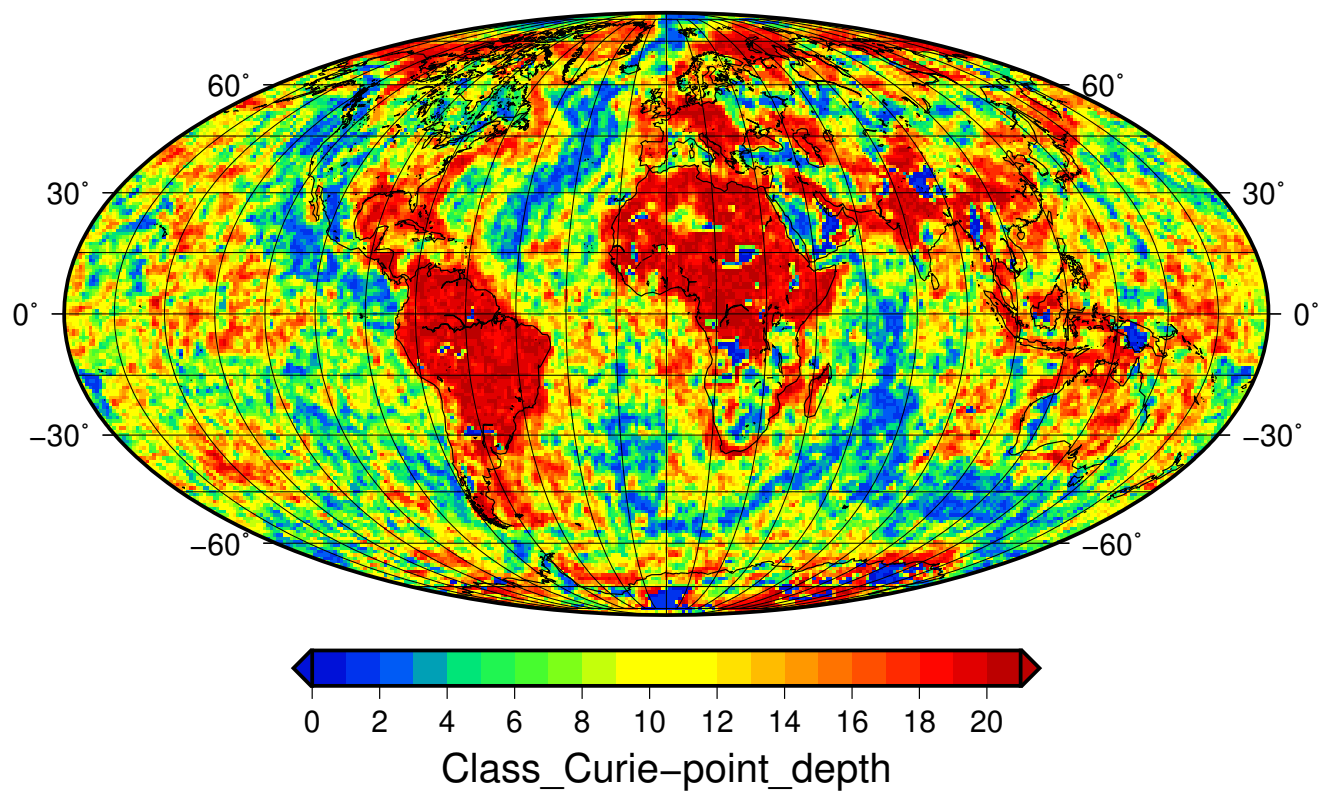
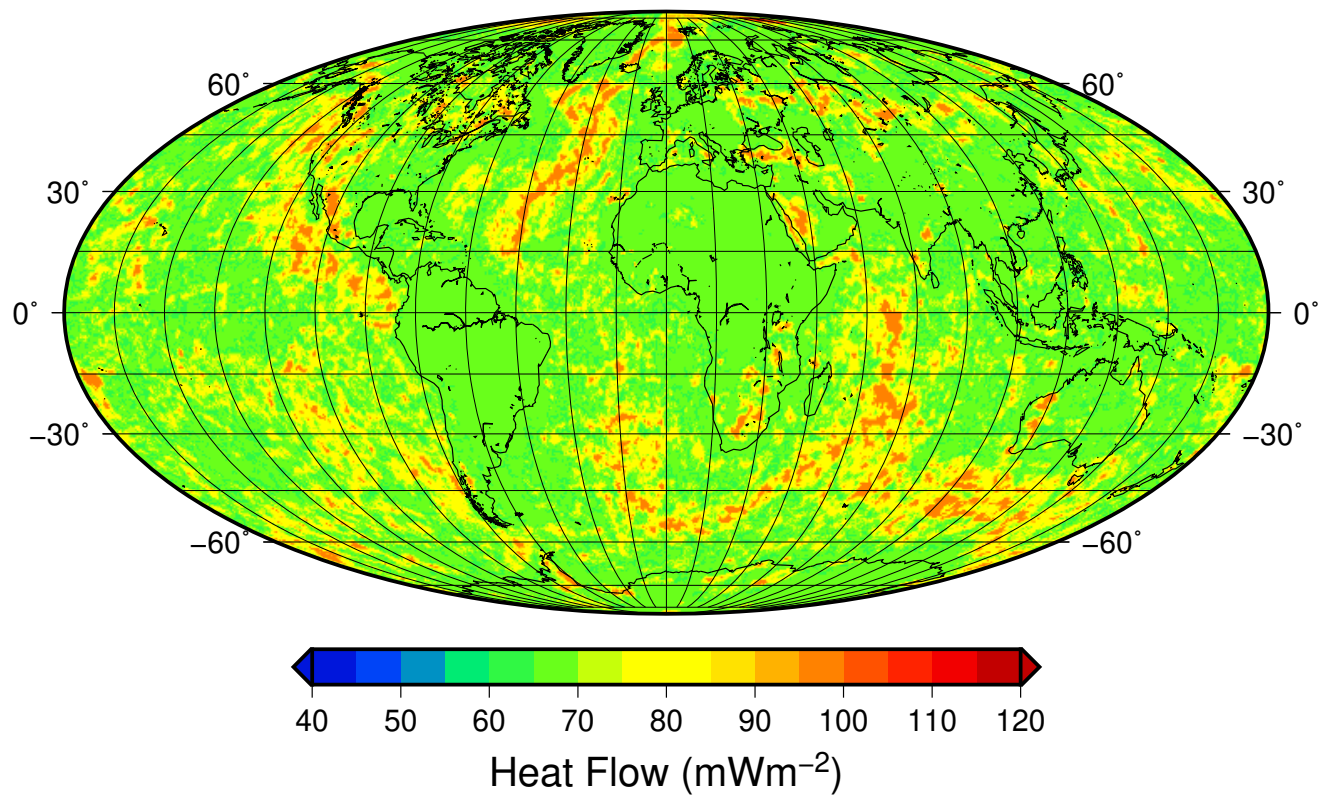
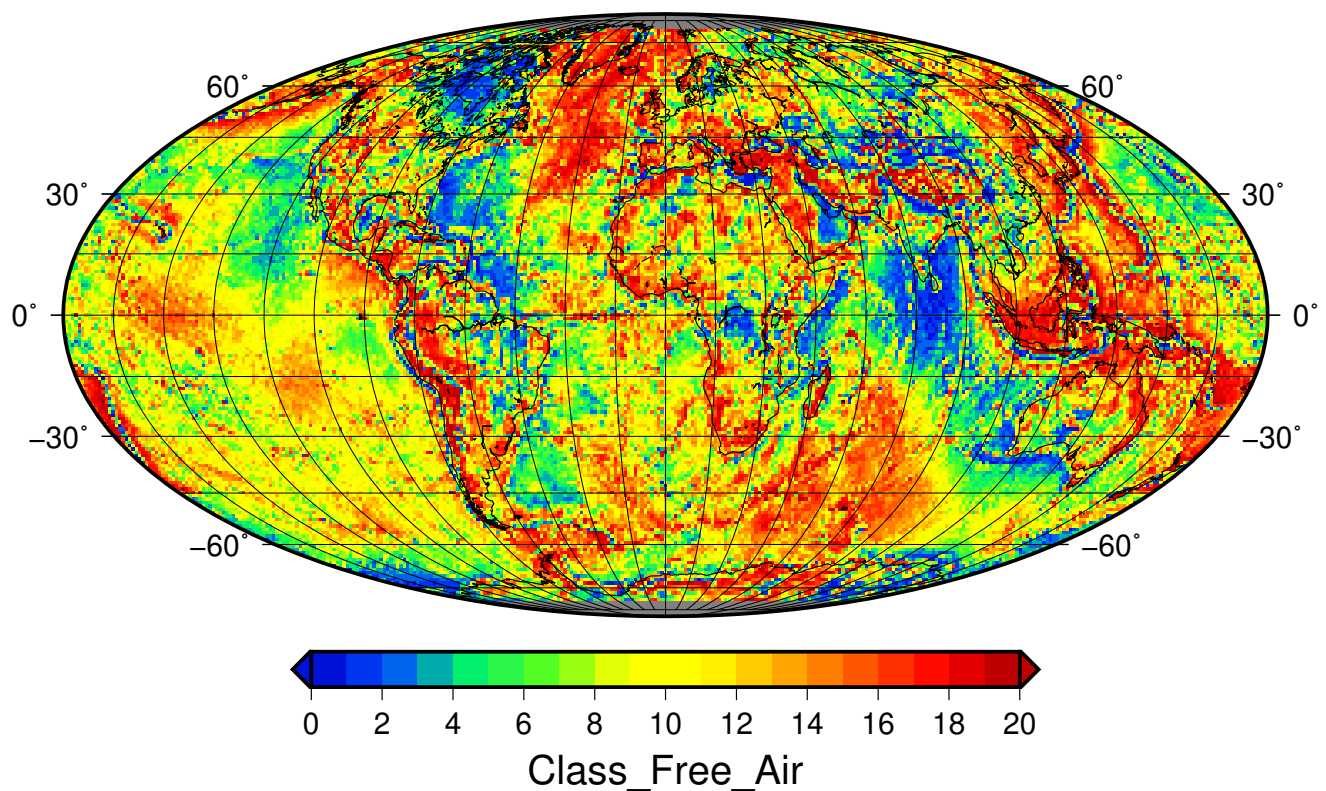
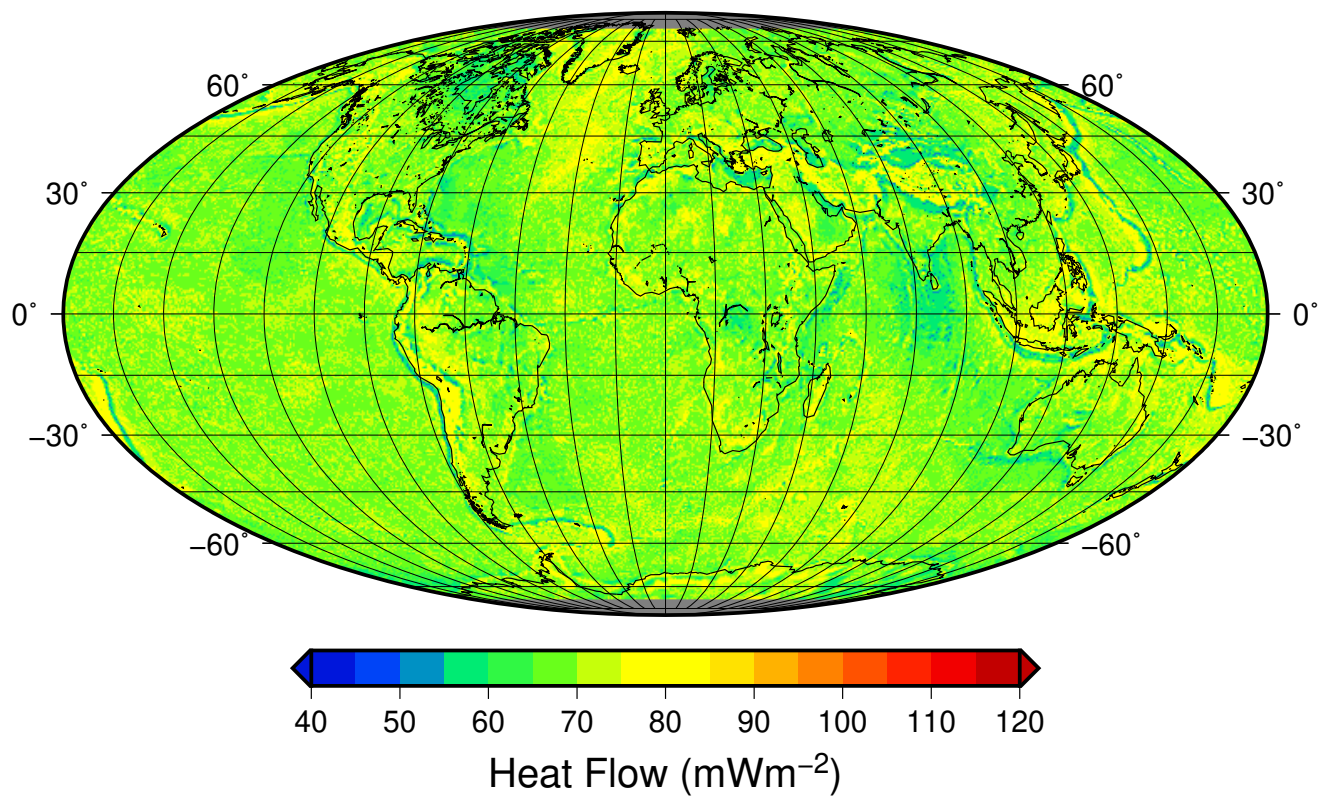


Figure S17. Curie depth classification after Li et al. (2017)



**Figure S18.** Free Air gravity classification after Sandwell and Smith (2009)

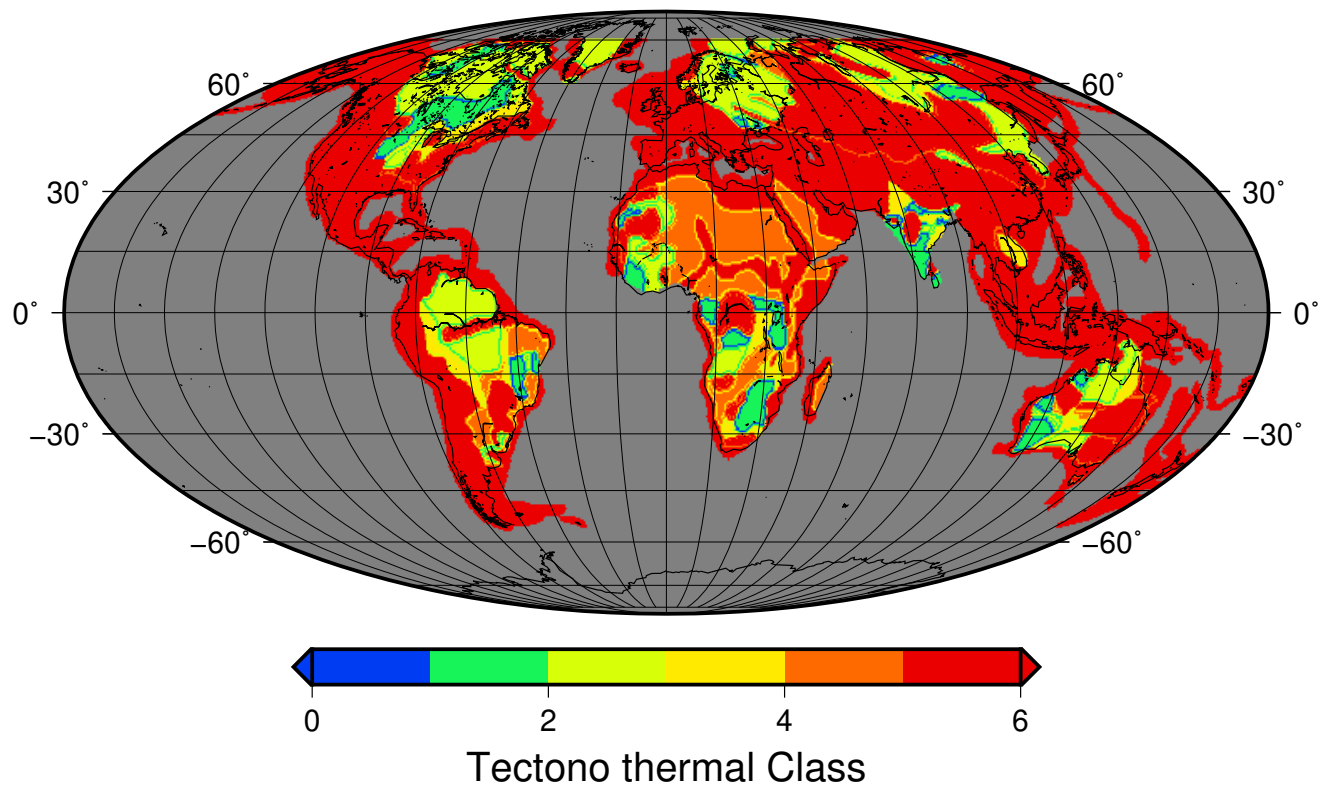
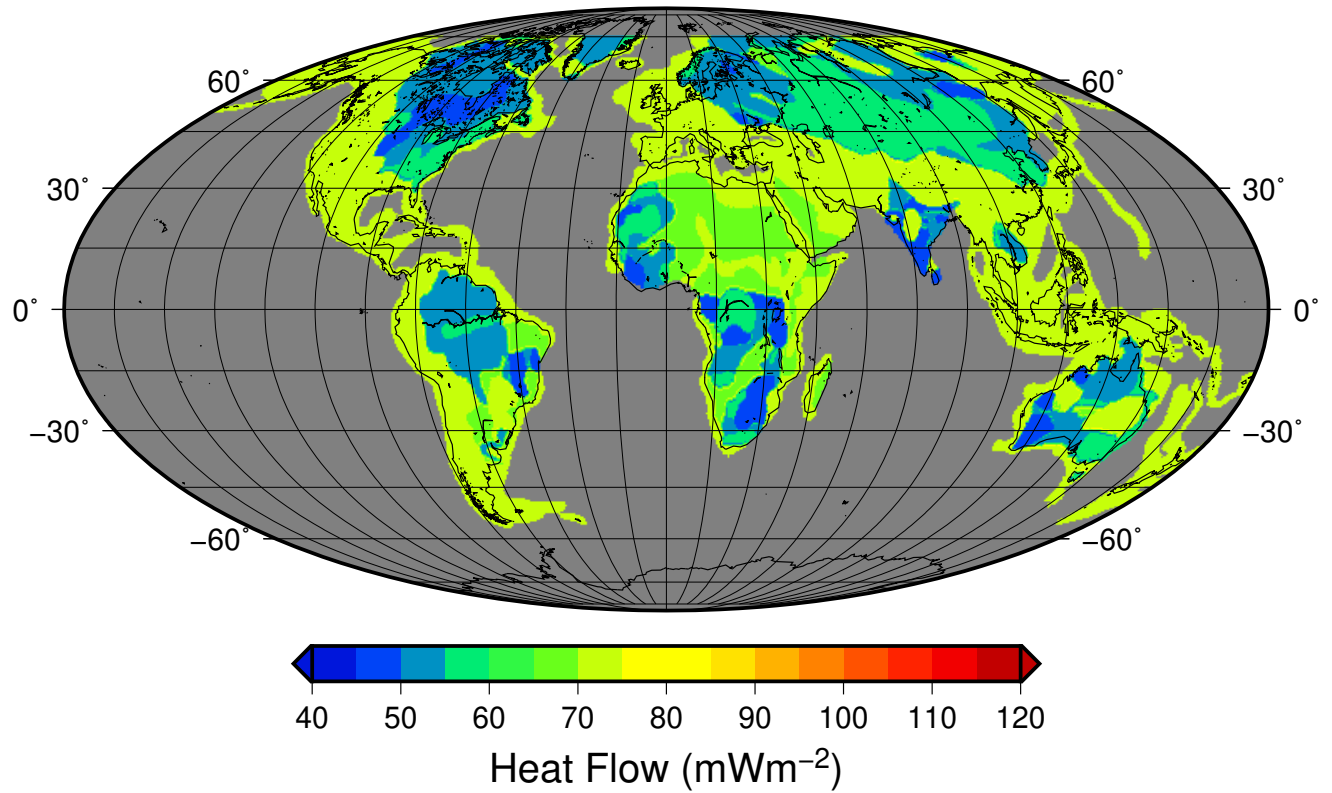


Figure S19. Last Tectono-thermal age (USGS, 1997)

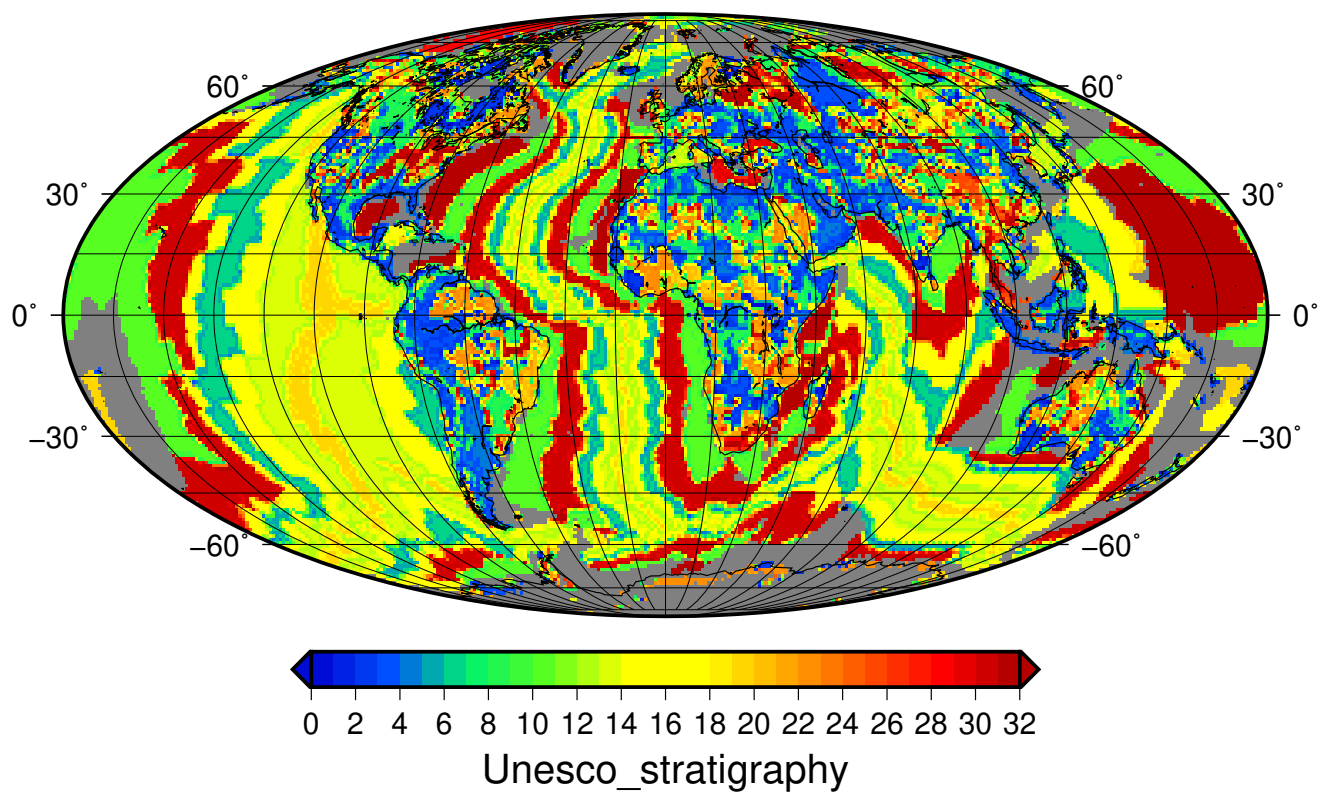
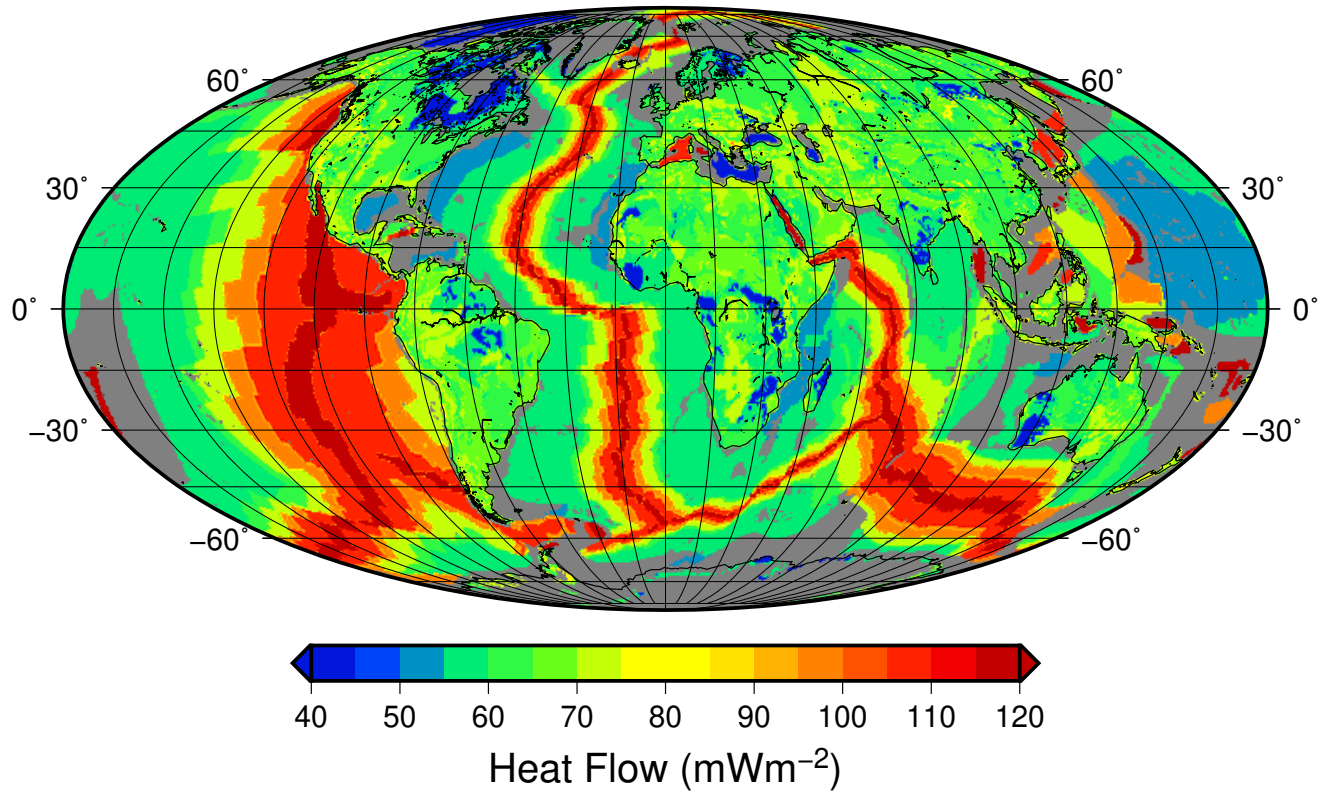


Figure S20. Global stratigraphy from CCGM/CGMW (2000)

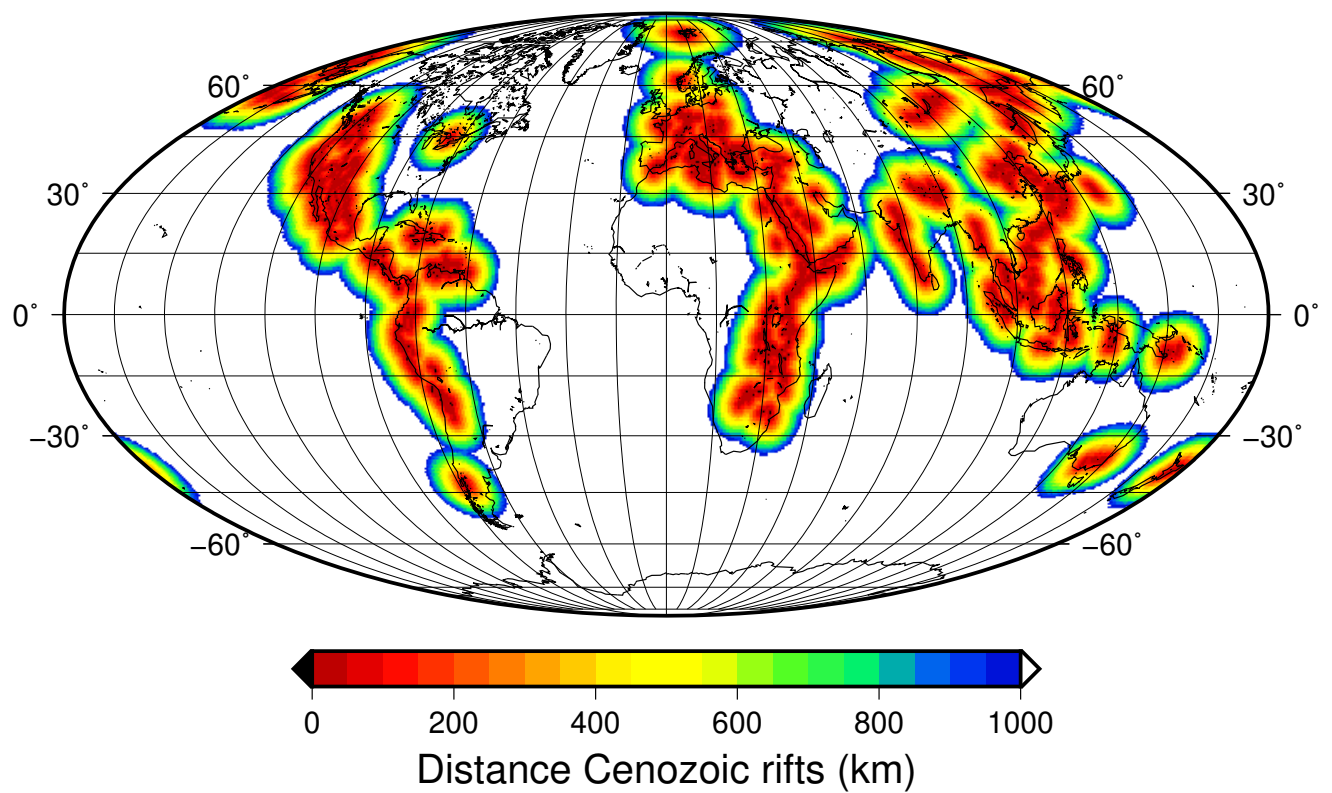
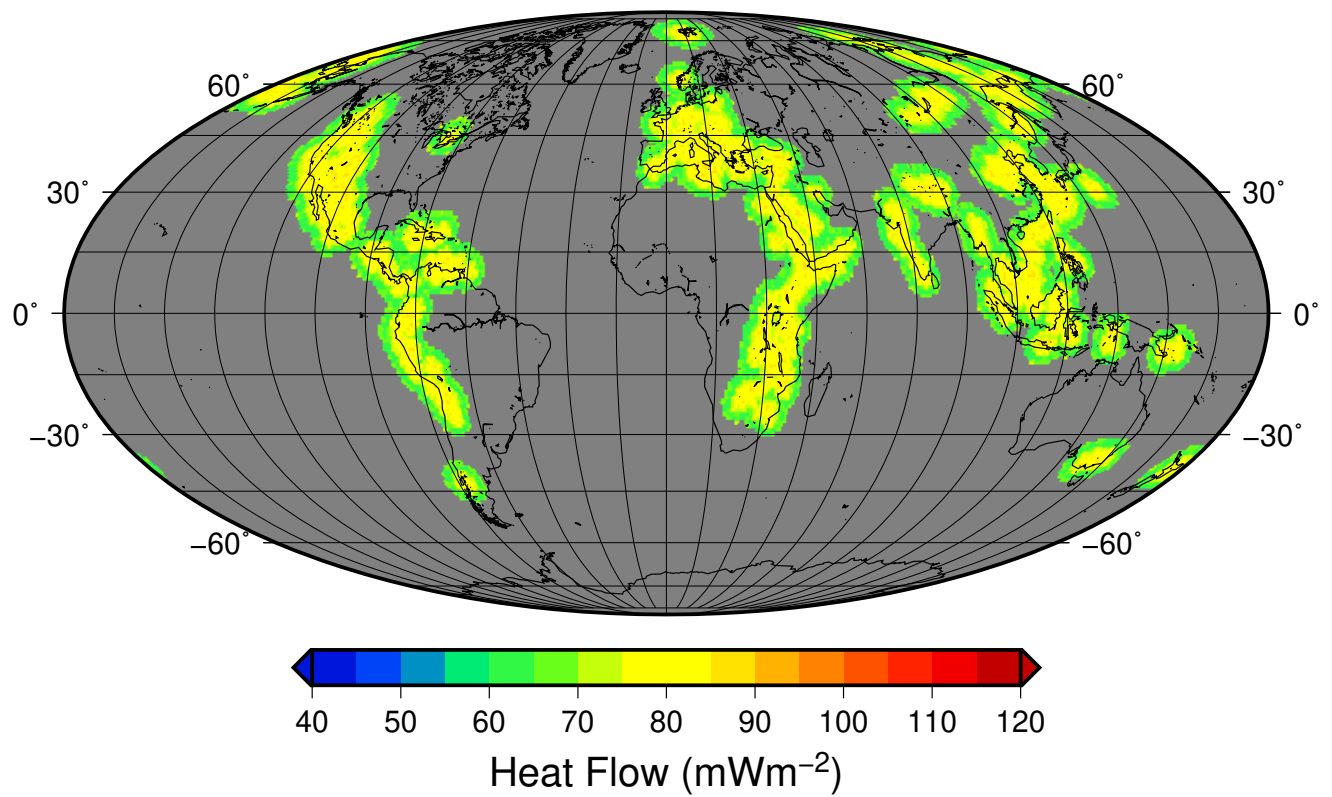


Figure S21. Distance to Cenozoic rifts

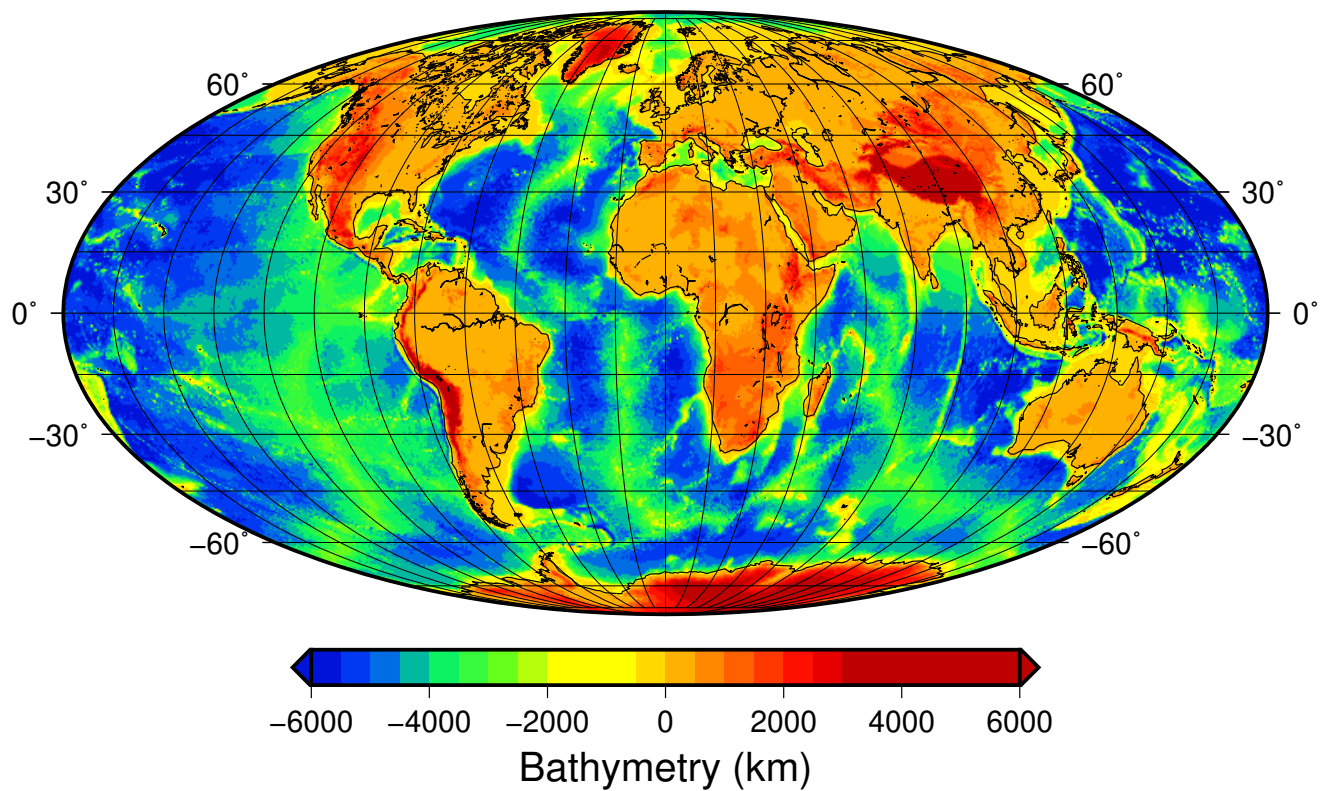
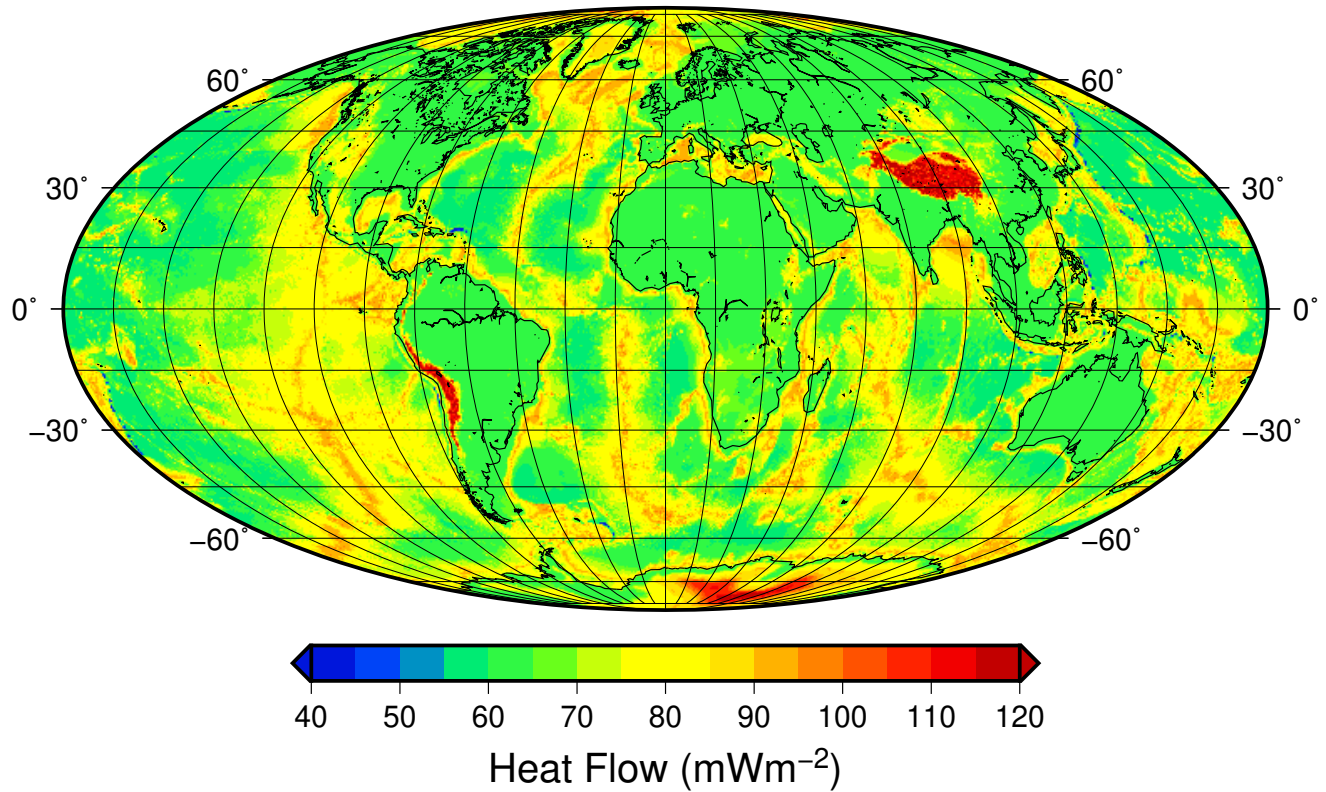


Figure S22. Earth topography and bathymetry (Kautz, 2017)

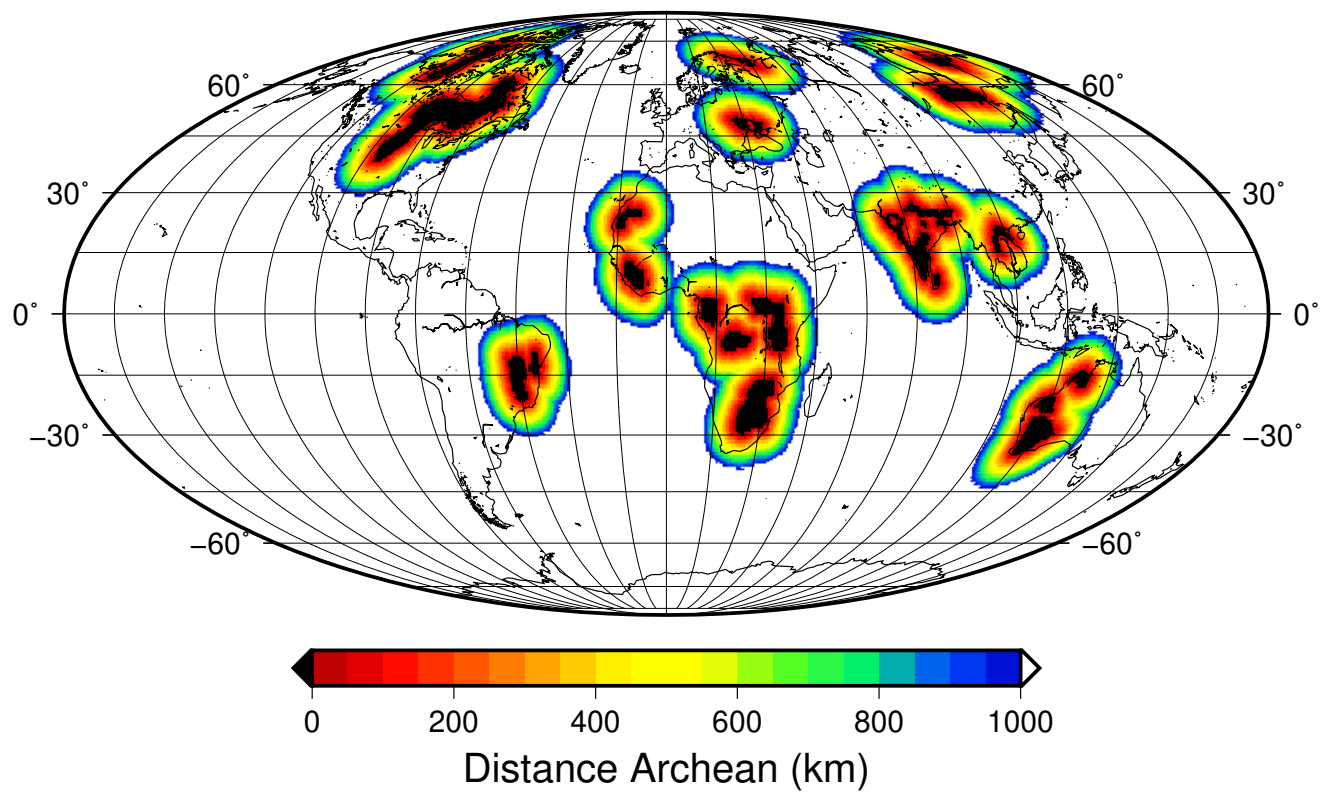
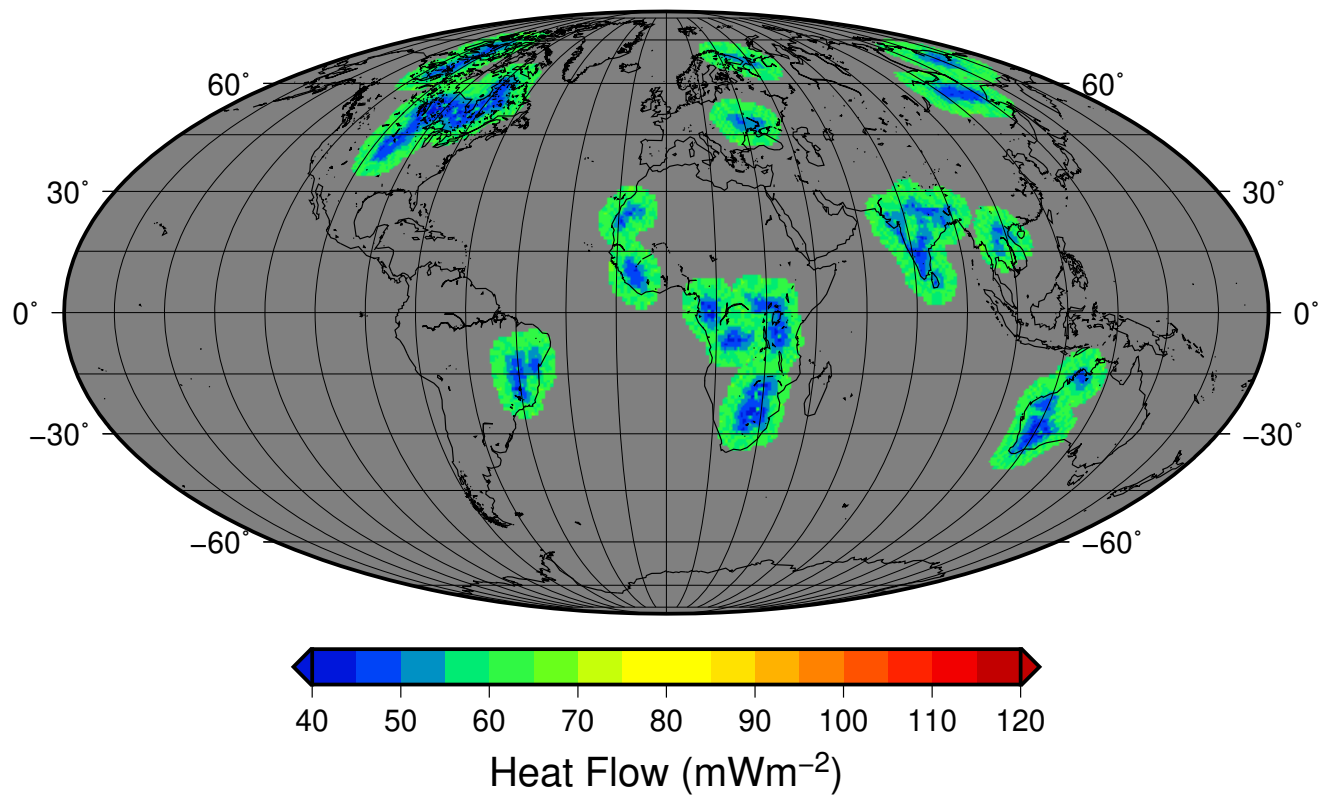


Figure S23. Average distance to Archean

**Table S1.** Code 1: Geography

A	Africa
B	North America
C	South America
D	Australia
E	Europe, Greenland
F	Miscellaneous lands, including New Zealand, Pacific Islands, Iceland, etc
G	Antarctica
H	Asia, Arabia, India
N	Atlantic ocean
O	Indian Ocean
P	Pacific Ocean
Q	Arctic Ocean
R	Mediterranean, Black and Caspian seas
S	Other marginal seas
X	Red Sea, Gulf of Suez, Gulf of Aden
Y	Southern Ocean
Z	not specified

**Table S2.** Code 2: Geology - Stratigraphy

A	Archean
B	Proterozoic
C	Phanerozoic non orogenic
D	Early Paleozoic orogeny
E	Late Paleozoic orogeny
F	Mesozoic orogeny
G	Tertiary orogeny
H	Geothermal area
N	Ocean basin
O	Ocean ridge or rise
P	Ocean trench
Q	Continental rise
R	Continental shelf
Y	Subduction
Z	Not specified
J	Active Margin
K	Back-Arc Basin
I	Continental Rifting
S	Strike-Slip
L	Foreland basin
M	Cratonic Basin

**Table S3.** Code 3: Type of temperature measurement

A	In borehole - all vertical boreholes
B	In mine - horizontal boreholes only
C	In tunnel - one level
D	In inclined boreholes
H	From BSR/ Gas Hydrates
L	In lake bottom by oceanographic techniques
N	Bullard or violin-bow type probe
O	Ewing or outrigger type probe
P	Other probes
Q	Deep sea borehole
W	Oil exploration (BHT or DST)
Z	not specified
G	Gravity Core
T	Thermal blanket (ridges)
M	Modeling

**Table S4.** Code 4: Type of conductivity estimate

A	Divided bar
B	Transient method in laboratory
C	Down-hole probe
D	Chips in divided bar
E	Other laboratory method
N	Needle probe
O	Water content
P	Chlorine content
Q	In-situ method
R	Other method
S	None
Z	not specified
M	from mineralogy / porosity
F	Optical scan
L	estimated

**Table S5.** Code 5: Type of corrections

A	Climatic change
B	Topographic irregularity
C	Sedimentation or erosion on land
D	Nearby bodies of water
E	water circulation
F	refraction by conductivity contrasts
G	composite corrections - land
H	None
I	Estimated by author to be zero or small
J	Rejected by compiler as being unreliable - uncorre...
N	Sedimentation
O	sea floor or lake topography and edge effects
P	water temperature variation
Q	composite corrections - sea - lake
R	None - sea
Z	Not specified
K	Horner-Plot, extrapolation to equilibrium conditio...
L	AAPG empirical correction
T	Tilt

**Table S6.** Code 6: Quality of measurements

A	Very Good (less than 10% variation of heat with de...
B	Good greater than 10% variation of heat with depth...
C	Average (less than 30% variation of heat with dept...
D	Data not used in heat-flow maps
Z	not specified

**Table S7.** Comparison of heat-flow data distributions between GLOBHEAT and NGHF databases for various grid cells. Heat-flow value corresponds to the areal weighted average.

Resolution (°)	Pollack et al. (1993)			this study		
	cells number	Area of Earth (%)	Heat-Flow ( $mWm^{-2}$ )	cells number	Area of Earth (%)	Heat-Flow ( $mWm^{-2}$ )
5×5	1,280	62.5	64.7	1,603	75.4	71.5
1×1	6,734	12.9	66.0	9,990	18.7	72.5
0.5×0.5	9,776	4.7	68.6	16,437	7.6	73.7

**Table S8.** Classes defining the Curie point depth

class	depth min. (km)	depth max. (km)
1	0.0	2.0
2	2.8	13.3
3	13.3	15.0
4	15.0	16.3
5	16.3	17.30
6	17.3	18.2
7	18.2	19.1
8	19.1	19.9
9	19.9	20.6
10	20.6	21.4
11	21.4	22.1
12	22.1	23.0
13	23.0	23.9
14	23.9	24.8
15	24.8	26.0
16	26.0	27.2
17	27.2	28.8
18	28.8	30.8
19	30.8	33.6
20	33.6	45.0
21	45.0	116.0

**Table S9.** Classes defining the Free Air Gravity (mgal)

class	depth min. (km)	depth max. (km)
1	-1000	-349 mgal
2	-349	-45.3 mgal
3	-45.3	-31.4 mgal
4	-31.4	-24 mgal
5	-24	-18.6 mgal
6	-18.6	-15.4 mgal
7	-15.4	-12.2 mgal
8	-12.2	-9.02 mgal
9	-9.02	-5.82 mgal
10	-5.82	-3.68 mgal
11	-3.68	-0.479 mgal
12	-0.479	1.66 mgal
13	1.66	4.86 mgal
14	4.86	8.06 mgal
15	8.06	12.3 mgal
16	12.30	16.6 mgal
17	16.60	23 mgal
18	23.00	31.5 mgal
19	31.50	49.7 mgal
20	49.70	1000 mgal

**Table S10.** Classes defining UNESCO lithology

class	type
1	Continental and island arc margins
2	Endogenous rocks (plutonic and/or metamorphic)
3	Extrusive volcanic rocks
4	Oceanic crust
5	Seamount, oceanic plateau, anomalous oceanic crust
6	Sedimentary rocks (or undifferentiated facies)

**Table S11.** Classes defining UNESCO stratigraphy

class	type
1	Archean
2	Cenozoic
3	Cenozoic - Quaternary
4	Continental and island arc margins
5	Eocene
6	Jurassic + Cretaceous - Mesozoic
7	Lower Cretaceous
8	Lower Paleozoic
9	Meso-Cenozoic (undifferentiated)
10	Miocene
11	Neogene
12	Oligocene
13	Paleocene
14	Paleozoic (undifferentiated)
15	Paleozoic + Mesozoic (undifferentiated)
16	Plio-Quaternary
17	Precambrian (undifferentiated)
18	Precambrian + Paleozoic (undifferentiated)
19	Proterozoic
20	Proterozoic + Paleozoic (undifferentiated)
21	Seamount, oceanic plateau, anomalous oceanic crust
22	Triassic - Mesozoic
23	Triassic - Mesozoic - Jurassic + Cretaceous
24	Undifferentiated Cretaceous
25	Undifferentiated Jurassic - Cretaceous
26	Upper Cretaceous
27	Upper Paleozoic
28	Upper-Middle Jurassic